nature communications

Article

https://doi.org/10.1038/s41467-025-59638-w

Targeted disruption of PRC1.1 complex enhances bone remodeling

Received: 14 November 2024

Accepted: 29 April 2025

Liangyu Xing[1,2,10], Jinxin Xu[3,4,10], Meihan Gong[1,2,10], Yunzhi Liu[1,2,10], Xuanyuan Li[1,2], Lingyu Meng[4,5], Ruyue Du[4,5], Ying Zhou[1], Zhaoguang Ouyang[1], Xu Liu[1], Shaofei Tao[1], Yuxin Cao[1], Chunyi Liu[1], Feng Gao[1], Ruohui Han[1], Hui Shen[5], Yan Dong[4,5], Yong Xu[3,4,5], Tao Li[6], He Chen[6], Yingying Zhao[2,6], Baoyou Fan[7], Lei Sui[1], Shiqing Feng[7,8] ✉, Jinsong Liu[5] ✉, Dayong Liu[1,9] ✉ & Xudong Wu[1,2,7] ✉

Polycomb repressive complexes (PRCs) are pivotal epigenetic regulators that preserve cell identity by restricting transcription responses to sub-threshold extracellular signals. Their roles in osteoblast function and bone formation remain unclear. Here in aging osteoblasts, we found marked activation of PRC1.1 complex, with KDM2B acting as a chromatin-binding factor and BCOR and PCGF1 enabling histone H2A monoubiquitylation (H2AK119ub1). Osteoblast-specific *Kdm2b* inactivation significantly enhances bone remodeling under steady-state conditions and in scenarios of bone loss. This enhancement is attributed to H2AK119ub1 downregulation and subsequent Wnt signaling derepression. Furthermore, we developed a small molecule termed iBP, that specifically inhibits the interaction between BCOR and PCGF1, thereby suppressing PRC1.1 activity. Notably, iBP administration promotes bone formation in mouse models of bone loss. Therefore, our findings identify PRC1.1 as a critical epigenetic brake on bone formation and demonstrate that therapeutic targeting of this complex enhances Wnt pathway activation, offering a promising strategy against skeletal deterioration.

The adult skeleton undergoes continuous bone remodeling, involving the resorption of mineralized bone by osteoclasts (OCs) and the subsequent formation of bone matrix by osteoblasts (OBs), which then become mineralized. This dynamic process is vital for maintaining skeletal integrity and ensuring mineral homeostasis. An imbalance between OBs and OCs leads to defective ossification, which in turn can result in conditions such as skeletal dysplasia or an increased risk of fractures[1,2]. The process of ossification is influenced by various factors, including nutrition, pharmaceuticals, hormones, inflammation, and mechanical stress on the bones, etc. Consequently, disorders such as trauma, infection, rheumatoid arthritis, postmenopausal osteoporosis and disuse osteoporosis often present with bone loss. The deterioration of skeletal integrity significantly raises the risk of pathological fractures and negatively impacts overall well-being.

OBs, as the primary bone-forming cells, play a crucial role in bone formation, maintenance, and remodeling through functions such as synthesizing the bone matrix, mineralization, producing signaling molecules and interacting with OCs[3,4]. To develop effective and safe therapeutics to modulate bone formation, it is crucial to decipher the molecular mechanisms that govern the differentiation and functionality of OBs.

Over the past two decades, genetic studies in humans and mice have consistently highlighted Wnt signaling as a critical driver for bone formation and regeneration[5,6]. Upon binding of Wnt ligands to their receptors, β-catenin is stabilized, translocated to the nucleus, and

---

A full list of affiliations appears at the end of the paper. ✉e-mail: sqfeng@tmu.edu.cn; liu_jinsong@gibh.ac.cn; dyliuperio@tmu.edu.cn; wuxudong@tmu.edu.cn

forms a complex with transcription factors such as TCF/LEF, thereby initiating the transcription of target genes in mesenchymal stem cells (MSCs) or OBs for osteogenesis[7]. TCF/LEF, in conjunction with lineage-specific factors like RUNX2 and OSTERIX/SP7, modulates OB differentiation and the expression of bone matrix genes[8–10]. Deficiency or mutations in Wnt ligands or their corresponding FZD and LRP receptors lead to significant impairments in bone formation[5,6,11,12]. Although numerous therapeutic strategies have been developed to target Wnt signaling components[5,6], their efficacy is contingent on the chromatin environment's responsiveness[13,14]. The epigenetic mechanisms that govern the transcriptional response to Wnt/β-catenin signaling and OB functions are not yet fully understood.

Among epigenetic repressors, Polycomb group (PcG) proteins have been demonstrated to restrict transcription response to extracellular cues[15] including Wnt signaling[16–19]. Through forming two biochemically distinct Polycomb Repressive Complexes (PRC1 and PRC2), they maintain a close chromatin environment through distinct activities. PRC2 catalyzes the methylation of histone H3 at lysine 27 (H3K27me), while canonical or non-canonical PRC1 complexes compact chromatin or catalyze monoubiquitylation of histone H2A at lysine 119 (H2AK119ub1) respectively[20,21]. PRC1 complexes share RING1 proteins (RING1A and RING1B) and are categorized into PRC1.1-PRC1.6 according to the composition of PcG ring-finger domain proteins (PCGF1-PCGF6). Canonical complexes PRC1.2 and PRC1.4 contribute minimally to H2AK119ub1 but play significant roles in chromatin compaction[22,23]. Non-canonical PRC1 bind chromatin through their unique DNA binding factors. In PRC1.1, FBXL10/KDM2B is responsible for recruiting the complex to CpG-rich promoters through its -CxxC domain[24,25], with BCOR and PCGF1 being essential accessory factors for H2AK119ub1 activity[26,27]. In PRC1.6, MAX/MGA contribute to chromatin binding while PCGF6 plays diverse roles in gene silencing or activation[28–30]. The specific expression patterns and functions of these PRCs in OBs remain largely unknown.

In this study, we observed an excessive activation of PRC1.1 complex in aging bones. Through generation of OB-specific KDM2B-deficient mouse models, we found that KDM2B inactivation leads to a significant increase of bone mass under physiological or ossification-defective conditions through enhanced bone remodeling. These osteogenic effects are dependent on the activation of Wnt signaling, associated with a decrease of H2AK119ub1 deposition at the Wnt/β-catenin target genes. Subsequently, we identified a compound specifically targeting PRC1.1 that limits H2AK119ub1 activity and activates Wnt signaling pathway. Furthermore, this compound promotes bone formation in vivo, presenting a promising epigenetic therapy for disorders characterized by bone deterioration.

Results

Gain of PRC1.1 function is linked to defective ossification during aging

Aging is a prevalent risk factor for bone loss, characterized by a continuous decline in OB activity. By comparing femurs from aged (18 months old) and young (3 months old) mice, we observed impaired ossification in the aged group, as evidenced by reduced trabecular bone revealed through micro-computed tomography (μCT) analysis (Fig. 1a).

To assess changes in gene expression, we performed RNA sequencing (RNA-Seq) analysis on primary OBs cultured in vitro for two weeks, focusing on the differentially expressed genes (DEGs). In aged OBs, 201 upregulated and 386 downregulated genes were identified relative to the young group (Fig. 1b and Supplementary Data 1). In line with these findings, the expression of numerous genes associated with aged OCs, as previously defined by Zhang et al.[31], was altered in aged OBs. These alterations included downregulation of genes such as *Alpl, Bglap, Bmp2* and upregulation of genes including *Ccr1, Ccl6* (Fig. 1c). Gene Oncology (GO) analysis of downregulated genes in aged OBs ($P < 0.05$) indicated a significant enrichment in ossification processes (Fig. 1d), underscoring the regulatory roles of identified genes in bone formation. The heatmap in Fig. 1e illustrates the downregulation of leading genes in ossification. Considering individual variability among mice, future studies should control for variables including genetic background, specific age, and environmental factors, to ensure reproducibility. These findings suggest that the reduction in bone mass is intimately linked to the diminished ossification capabilities of OBs. Investigating the specific contributions of these mouse-specific features will also be crucial for translating our findings to broader biological contexts.

Recognizing the established suppressive roles of PRCs on osteogenic signaling during OB differentiation[32,33], we compared the protein levels of PRC components in OBs isolated from mice of varying ages. As expected, Western Blot (WB) analysis revealed a significant rise in P16 expression levels with aging, a hallmark of cell senescence[34]. For reasons that remain to be elucidated, there was a noticeable decrease in the protein levels of EZH2 and SUZ12, which are core components of PRC2. Among the principal PRC1 members, RING1B levels showed a slight increase with age, while the levels of NSPc1/PCGF1 and KDM2B[25,35], were significantly elevated. In alignment with these findings, there was a specific and substantial increase in H2AK119ub1 levels and a modest decrease in H3K27me3 levels in aging OBs. The gain of H2AK119ub1 is primarily attributed to elevated levels of PCGF1, as other key members of non-canonical PRC1, such as PCGF3 and PCGF6, show either unchanged or only minor downregulation in expression (Fig. 1f, g). These data link the marked activation of PRC1.1 to bone aging.

Genome-wide profiling through Cleavage Under Targets and Tagmentation (CUT&Tag) analysis with proper spike-in normalization demonstrated a widespread increase of H2AK119ub1 signals in aged OBs compared to the young group (Fig. 1h and Supplementary Data 2). Among the 386 downregulated genes in aged OBs, we observed a significant elevation of H2AK119ub1 enrichment (Fig. 1i). Ossification genes serve as illustrative examples while the unaffected gene *Actin* serves as a negative control (Fig. 1j, k). Collectively, these findings suggest that PRC1.1 activation raises the threshold for transcriptional activation by osteogenic signals, thereby suppressing the ossification process.

KDM2B inactivation in OBs leads to enhanced bone formation

To investigate whether PRC1.1 limits OB functions, we managed to generate a mouse model of conditional ablation of PRC1.1. Accordingly, we created the conditional knockout allele of *Kdm2b* by flanking exon13 that encodes the CxxC-domain with two loxP sequences (Supplementary Fig. 1a)[18]. These floxed mice *Kdm2b*$^{flox/flox}$ were then crossed with the widely used OB-targeting *Ocn*-Cre mice to generate *Kdm2b*$^{fl/fl}$*Ocn*^{Cre} conditional knockout mice (referred to as CKO mice) (Fig. 2a and Supplementary Fig. 1b). This crossbreeding enabled the specific deletion of the KDM2B-CxxC domain, thereby abrogating its chromatin regulatory activity[25,36] in OBs. Notably, CKO mice showed no discernible differences in body size or weight compared to *Ocn*-Cre mice, referred to as control (CON) at various ages, including 9 and 10 weeks and between 6 to 12 months (Supplementary Fig. 1c).

Strikingly, at around 10 months of age, the femur length of CKO mice was significantly increased (Fig. 2b), suggesting potential alterations in the bone's internal structure. μCT analysis revealed a substantial enhancement in trabecular bone volume in CKO mice at various ages, with three-dimension (3D) reconstruction at 9 weeks of age (Supplementary Figs. 1d and 2c). Bone metrological analysis demonstrated significant increases in trabecular number (Tb.N), thickness (Tb.Th), and bone volume/total volume (BV/TV) ratio, along with a significant reduction in trabecular separation (Tb.Sp) in CKO mice (Fig. 2d). Hematoxylin-Eosin (H&E) staining of distal femur sections confirmed the increased bone mass in CKO mice (Fig. 2e).

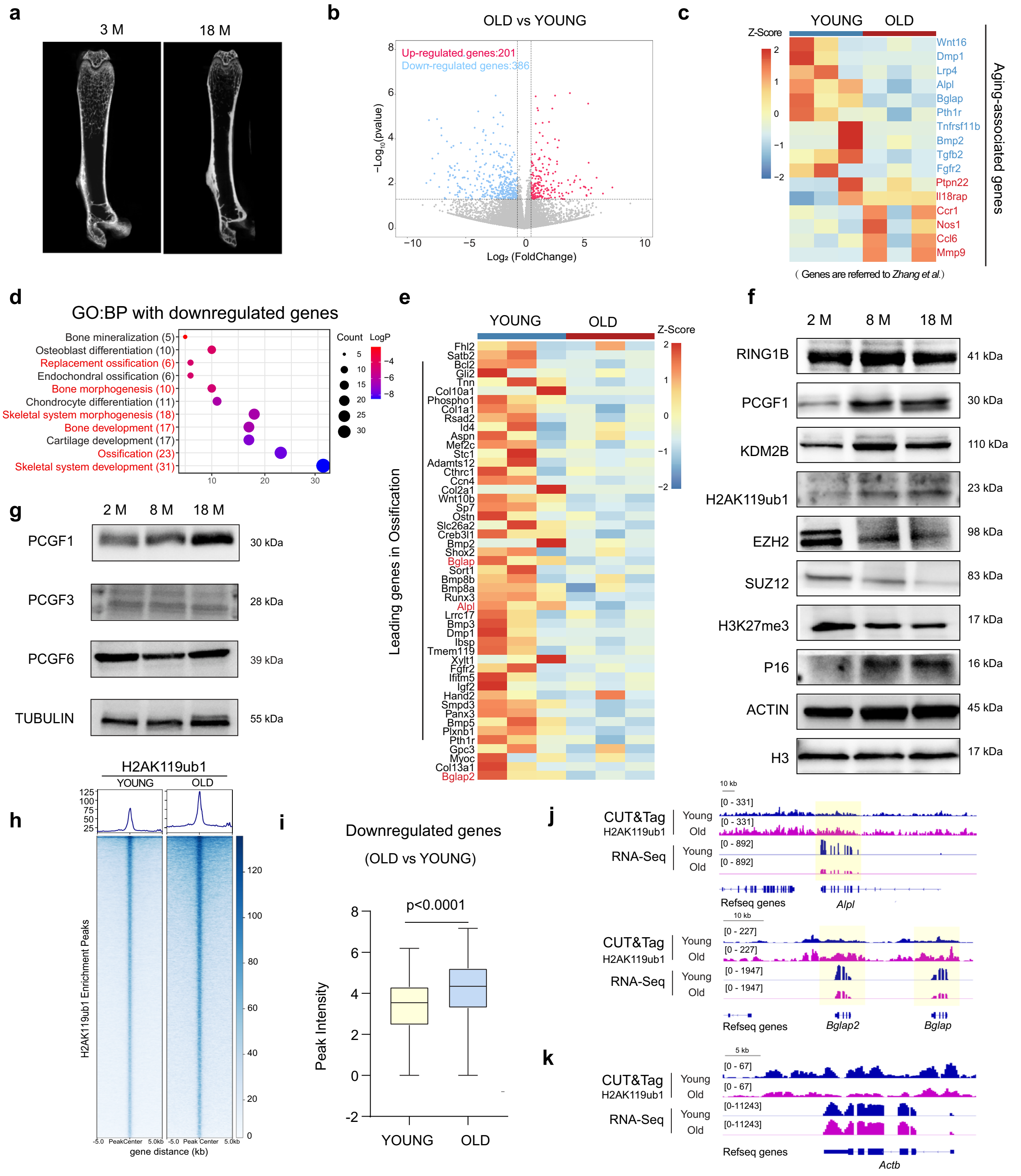

Fig. 1 | An aberrant gain of PRC1.1 function is linked to impaired ossification. **a** Representative images of scanning sections of mouse femurs at ages of 3 and 18 months. **b** Volcano plot of DEGs in OBs ($n = 3$ YOUNG and $n = 3$ OLD). Upregulated genes are labeled in red and downregulated genes in blue (Wald test, $p < 0.05$; |Fold change| >1.5). OBs were collected after 14 days of culture by removing the bone fragments. **c** Heatmap showing mRNA levels of osteocyte aging-associated genes between the two groups, colorscale: *Z*-Score. **d** GO enrichment analysis of the biological processes in downDEGs in aged OBs (Fisher's exact test, $p < 0.05$). Number of genes and statistical significance are shown. **e** Heatmap showing mRNA levels of ossification-related genes between the two groups. Colorscale: *Z*-Score. **f**, **g** WB analyses comparing the levels of PRC members and associated histone modifications in OBs from young and aged mice. ACTIN and H3 were used as loading controls, respectively. **h** Heatmaps showing H2AK119ub1 signals in chromatin of YOUNG and OLD OBs around the peak center (± 5 kb) of H2AK119ub1 target genes. Colors represent CUT&Tag RPM, and rows were ranked by CUT&Tag signals in young group ($n = 2$ YOUNG and $n = 2$ OLD). OBs were collected after 14 days of culture by removing the bone fragments. **i** Boxplots showing quantification of differential H2AK119ub1 enrichment at downDEGs (OLD vs YOUNG, $n = 386$, Wilcoxon matched-pairs signed rank test, two tailed, $p < 0.0001$). The boxplots indicate the median (centre line), the third and first quartiles (box limits) and 1.5 × IQR above and below the box (whiskers). **j**, **k** The IGV view of increased H2AK119ub1 enrichment at the promoter of representative ossification-related genes and their decreased mRNA levels in aged OBs compared with young group, with Actin serving as a negative control. Signals representing CUT&Tag and RNA-seq RPM. 2 M: 2 months; 3 M:3 months; 8 M:8 months; 18 M:18 months. Source data of (**f**, **g**, **i**) are provided as a Source Data file.

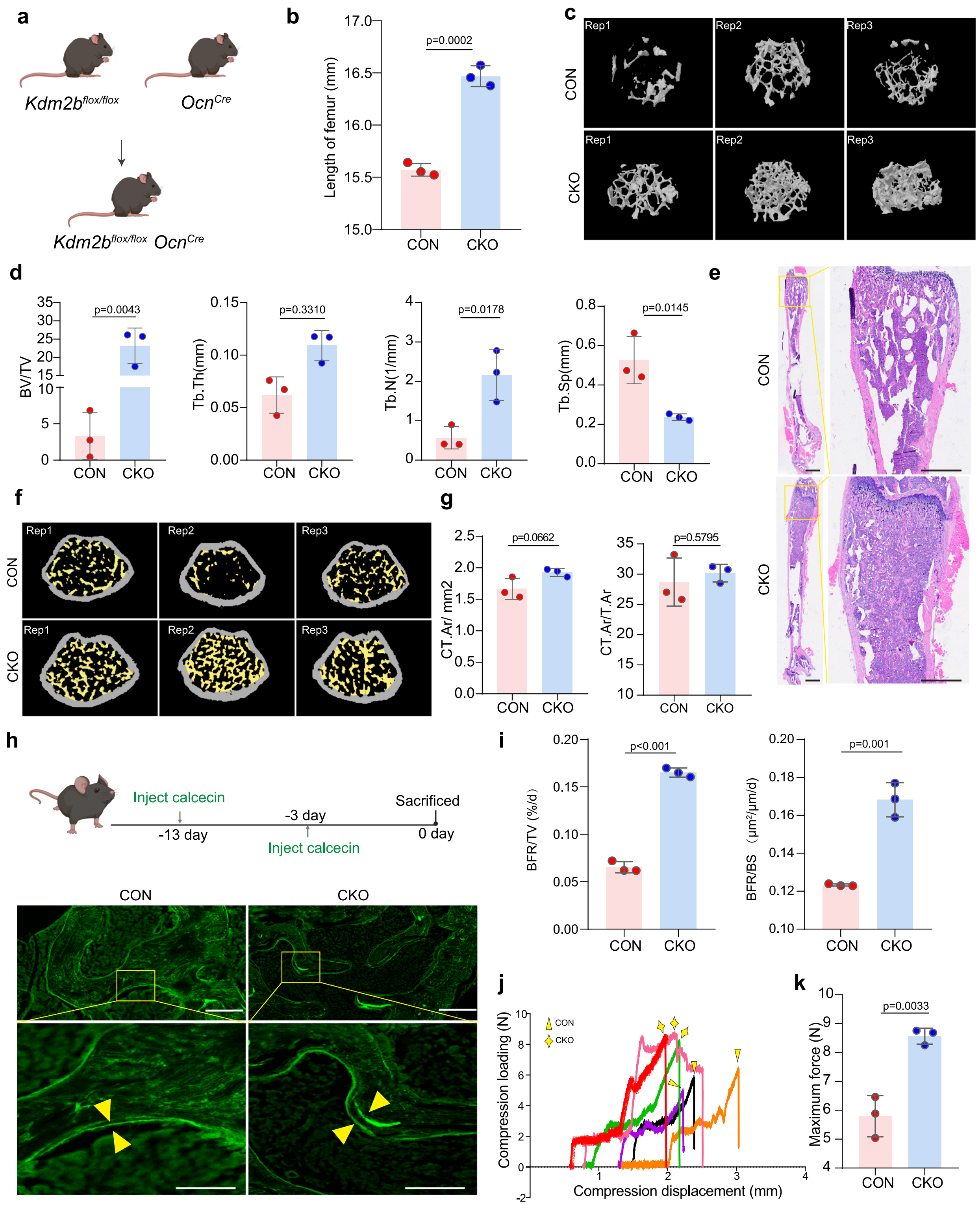

Fig. 2 | KDM2B inactivation in OBs leads to increased bone mass and enhanced bone formation. **a** Schematic diagram of construction of CKO mice. **b** Statistical analysis of femur length of 9-week-old mice ($n = 3$ per genotype). **c** Representative images of 3D reconstruction and scanning sections of femurs from control and CKO mice at the age of 9 weeks. **d** μCT analysis of trabecular parameters ($n = 3$ per genotype). **e** Representative images of H&E staining of the whole femur (left) and metaphysis (right) from CKO and control mice. **f** Representative images of femurs from control and CKO mice, the yellow areas represent trabecular bone and the gray areas represent cortical bone. **g** μCT analysis of cortical bone parameters ($n = 3$ per genotype). **h, i** Schematic diagram of the timeline of the calcein double labeling experiment. Representative images (**h**) and quantification of calcein double labeling parameters (**i**) ($n = 3$ mice per genotype). **j** Three-point bending experiment, with blue arrows indicating the CKO group and yellow arrows indicating the CON group. **k** Statistical analysis of the maximum load bearing capacity of fresh unfixed femurs from three-point bending tests ($n = 3$ mice per genotype). Statistical significance was assessed using Student's *t* tests, two-tailed, in (**b**, **d**, **g**, **i**, **k**), error bars are presented as mean values ± SD. Scale bar, 1 mm in (**e**) and 100 μm in (**h**). CON: *Ocn-Cre* CKO: *$Kdm2b^{fl/fl}$ Ocn-Cre*, (**a**) and (**h**) created with Biorender (https://biorender.com/w07p252, https://BioRender.com/ibb92gm). Source data of (**b**, **d**, **e**, **g**, **i**, **j**, **k**) are provided as a Source Data file.

Heterozygous (HE) mice, however, showed no apparent differences in trabecular bone architecture compared to the control group (Supplementary Fig. 1e). In contrast to trabecular bone, no significant differences in cortical bone were observed between CKO and control mice, as evidenced by the lack of statistical variation in absolute or relative Cortical bone Area (Ct.Ar) (Fig. 2f, g). Thus, these data reveal a role for KDM2B in the negative regulation of trabecular bone mass.

To directly assess new bone formation, we administered calcein injections 13 days and 3 days prior to the mice sacrifice, followed by the visualization of fluorescent bands (Fig. 2h). According to the distance between double labels of mineralization, the bone formation rate/bone surface (BFR/BS) and bone formation rate/total volume (BFR/TV) were significantly increased in CKO mice (Fig. 2i). Additionally, we compared the structural integrity of femurs from CKO and control mice using a three-point bending test. By comparing the compression loading, we noticed that the CKO femurs could withhold significantly higher forces (Fig. 2j, k), indicating enhanced bone stiffness compared to controls.

Notably, tartrate-resistant acid phosphatase (TRAP) staining of femurs unveiled a significant increase in the number of OCs in CKO mice as measured by OC per tissue area (N.Oc/T.Ar) (Supplementary Fig. 1f, g). Moreover, the serum levels of RANKL, a well-recognized bone resorption factor were significantly elevated in CKO mice (Supplementary Fig. 1h). These data support that the enhanced bone density observed in CKO mice is not due to decreased bone resorption but attributed to elevated OB function and augmented bone formation. Consistent with this, OB-secreted RANKL has been shown to induce OC differentiation[13]. Therefore, these findings indicate that KDM2B limits bone remodeling under steady states.

KDM2B inactivation boosts OB functions to prevent bone loss and enhance bone repair

Next, we wondered how KDM2B-inactive OBs respond to diverse microenvironments of defective ossification. Initially, we compared the bone architecture of the femur between CKO mice and WT mice at 18 months of age. µCT scanning unveiled that the trabecular bone loss observed in control mice was significantly mitigated in CKO mice (Fig. 3a). A substantial increase in BV and Tb.N, along with a decrease in Tb.Sp, was noted in CKO mice relative to the control group, though Tb.Th remained unchanged (Fig. 3b). Furthermore, to model post-menopausal osteoporosis, we performed ovariectomy (OVX) on both CON and CKO mice. µCT analysis indicated that CKO mice demonstrated significant resistance to OVX-induced bone loss (Fig. 3c, d). Thus, KDM2B-inactivated OBs effectively counteract bone loss associated with aging or hormonal deficiency.

To determine how KDM2B-deficient OBs react to acute stimuli, we created a circular bone defect (1-mm diameter) in the midshaft of the femur using low-speed dental handpieces in both CON and CKO mice (Supplementary Fig. 2a, b). As shown in Fig. 3e, CKO mice exhibited a greater presence of bone-like substances around the circular defects compared to the CON group. The BV/TV value of newly formed bone was approximately three times higher in CKO mice than in the CON group (Fig. 3f). Sagittal plane H&E staining clearly confirmed increased osteoid and new bone formation in CKO mice following acute bone trauma (Fig. 3g). Moreover, TRAP staining revealed a significant increase in the number of OCs in new bone, suggesting an enhanced bone turnover in CKO mice (Supplementary Fig. 2c, d). Consequently, the heightened OB functionality due to KDM2B inactivation not only prevents bone loss but also expedites the bone repair process after acute trauma.

KDM2B inactivation enhances OB functions via Wnt/β-catenin signaling

Subsequently, we confirmed that KDM2B deficiency indeed results in the suppression of PRC1.1 activity. To accurately quantify the transcriptomic and epigenomic alterations following KDM2B inactivation, we utilized highly purified OBs for high-throughput sequencing analysis. To achieve this, we crossed *Ocn*^{Cre} or *Kdm2b*$^{fl/fl}$ *Ocn*^{Cre} mice with Ai14 reporter mice, which enables OB-specific expression of tdTomato following Cre-mediated recombination (Fig. 4a).

After genotyping (Supplementary Fig. 3a), the phenotype of the femur in CKO-tdTomato mice was confirmed by µCT (Supplementary Fig. 3b). The numbers of tdTomato-positive OBs were increased in both the trabecular and cortical bone of CKO mice (Fig. 4b, c), suggesting that the enhanced OB function also stimulates OB differentiation as positive feedback. Femurs from CON and CKO-tdTomato mice were minced into small fragments for OB culture. Within a few days, tdTomato-positive cells were observed migrating out of the cultured bone fragments (Supplementary Fig. 3c). Immunofluorescence (IF) staining confirmed the expression of RUNX2 and ALP, two osteogenic markers, in tdTomato-positive cells (Supplementary Fig. 3d). The adherent cells were subsequently harvested and collected after 14 days of culture, sorted by flow cytometry, and subjected to RNA-Seq analysis (Fig. 4d).

In either young or aged CKO OBs, hundreds of DEGs were identified compared to their respective controls (Fig. 4e, Supplementary Fig. 3e and Supplementary Data 3). Notably, 43% of the aged OB-downregulated genes (166 out of 386) are upregulated in aged CKO group (Supplementary Fig. 3f). GO analysis indicated the involvement of upregulated genes in young and old CKO OBs with skeletal system morphogenesis, embryonic skeletal system development, and skeletal system development (Fig. 4f and Supplementary Fig. 3g). RT-qPCR analysis confirmed the upregulated expression of osteogenic genes (Fig. 4g) in CKO OBs. Collectively, these analyses demonstrate that KDM2B ablation significantly reverses the deterioration of OB functions. Given the partial reversing effect, further studies are warranted to elucidate the interplay between PRC1.1 and other regulatory mechanisms in the context of aging.

Kyoto Encyclopedia of Genes and Genomes (KEGG) analysis showed that upregulated genes were enriched in Wnt signaling pathways (Fig. 4h and Supplementary Fig. 3g). As illustrated by heatmap and confirmed RT-qPCR analysis, multiple components of the Wnt pathway, including ligands, receptors, and signal transducers, were significantly activated upon KDM2B loss (Fig. 4i, j). Moreover, protein levels of β-catenin were increased in both femur tissues and tdTomato-positive OBs from CKO mice (Fig. 4k). To quantify the subcellular distribution of β-catenin, we separated nucleoplasmic and cytoplasmic fractions of OBs. WB analysis showed that β-catenin levels were significantly increased in the nucleus and slightly decreased in the cytoplasm (Fig. 4l).

Runx2 and *Sp7* recognized as osteogenic target genes downstream of β-catenin[8,13], were further investigated for their regulation by KDM2B. We overexpressed KDM2B-WT and KDM2B-ΔCxxC mutant in 3T3-E1 cells, a pre-OB cell line (Fig. 4m), and induced OB differentiation. Chromatin Immunoprecipitation (ChIP)-qPCR analysis of the differentiated cells revealed a significant increase of β-catenin binding at the *Runx2* and *Sp7* promoter regions in the KDM2B-ΔCxxC mutant group when compared to the KDM2B-WT group (Fig. 4n). These data suggest that KDM2B ablation strengthens the Wnt signaling pathway.

To substantiate the roles of activated Wnt signaling in OB functions, we treated the CKO mice with LGK974, a potent and specific inhibitor blocking WNT secretion[37,38]. After two weeks of LGK974 intraperitoneal injection (3 mg/kg), IF staining confirmed decreased β-catenin intensity in OBs (Supplementary Fig. 3h). µCT scanning showed that trabecular bone was significantly reduced by LGK974 treatment. Statistical analyses for trabecular bone microarchitecture unveiled a significant decrease in BV/TV, Tb.Th, and Tb.N and unchanged Tb.Sp (Fig. 4o, p). These data confirm the essential role of Wnt signaling in the enhanced OB functions resulting from KDM2B inactivation.

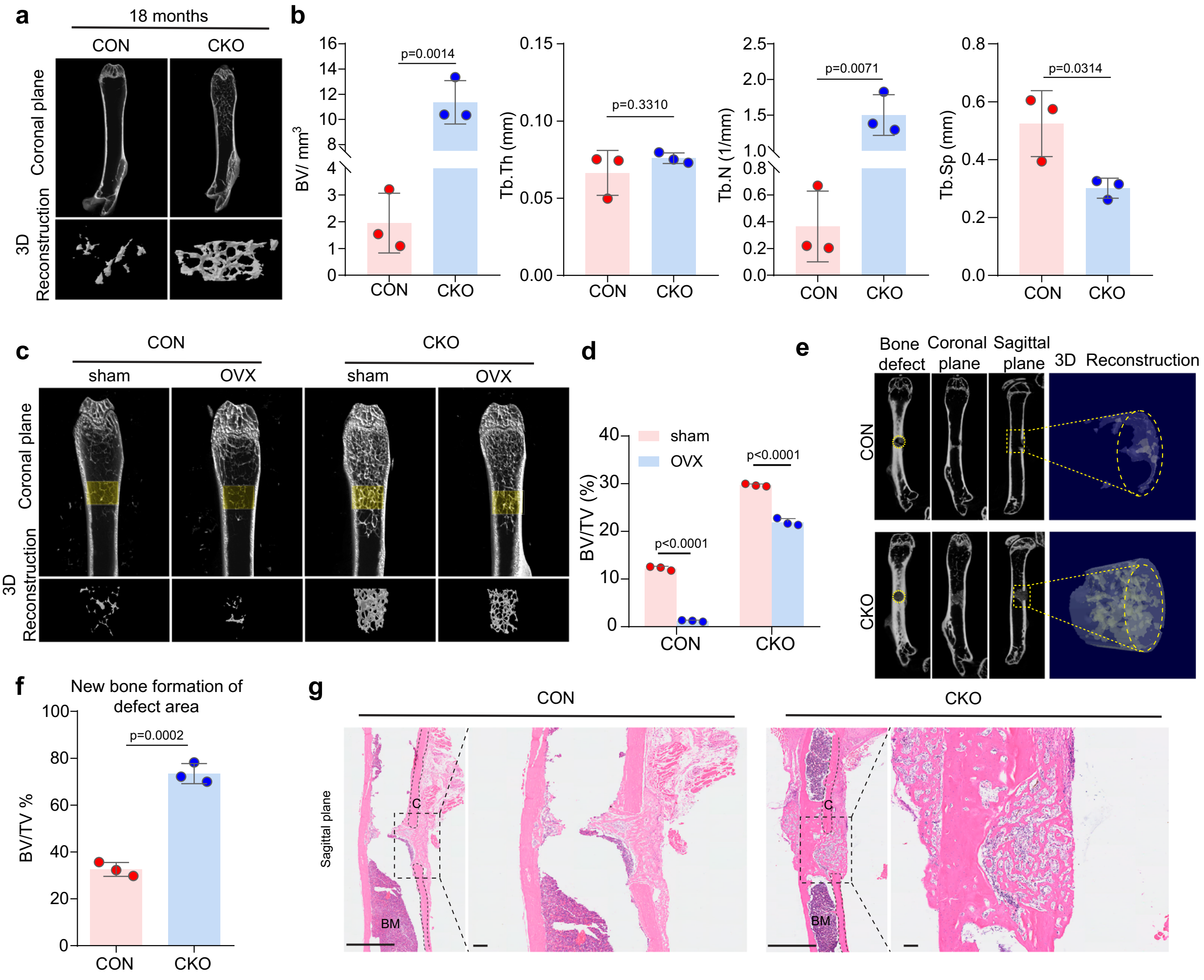

Fig. 3 | KDM2B inactivation boosts OB functions to counteract bone loss and enhance bone repair. a Representative images of 3D reconstruction and scanning sections of femurs from control and CKO mice at the age of 18 months. **b** µCT analysis of trabecular parameters ($n = 3$ mice per genotype). **c** Representative images of three-dimensional reconstruction and scanning sections of trabecular bone from OVX-CON, OVX-CKO, sham-CON, sham-CKO. **d** Statistical analysis to compare the BV/TV ratio in designated groups ($n = 3$ mice per genotype). **e** Representative images of scanning sections in coronal and sagittal plane of femur of bone defects (three columns on the left) and images of 3D reconstruction of repaired circular bone defect (column on the right) from control and CKO mice. **f** µCT analysis of BV/TV ratio of newly formed bone between control and CKO group ($n = 3$ mice per genotype). **g** Representative images of H&E staining of femur of repaired bone defect from control and CKO mice, box areas shown at a higher magnification. (C cortex, BM bone marrow). Statistical significance was assessed using Student's t tests, two-tailed, in (**b**, **f**), error bars are presented as mean values ± SD. Statistical significance was assessed using Two-Way ANOVA, two-tailed, in (**d**), error bars are presented as mean values ± SD. Scale bar, 1 mm in low-power field and 100 µm in high-power field of 3 g. sham, sham operation. OVX, Ovariectomy. CON *Ocn-Cre*, CKO $Kdm2b^{fl/fl}$ *Ocn-Cre*. Source data of (**b**, **d**, **f**, **g**) are provided as a Source Data file.

H2AK119ub1 loss in KDM2B-inactive OBs is associated with the Wnt/β-catenin target gene derepression

To find out whether the enhanced Wnt signaling in KDM2B-deficient OBs is attributed to the dampened function of PRC1.1, we simultaneously performed H2AK119ub1 CUT&Tag analysis (Fig. 4d). As expected, H2AK119ub1 levels at the promoters of 763 genes were significantly reduced in CKO OBs (Fig. 5a, b and Supplementary Data 4). Integrating these results with RNA-seq data revealed significant upregulation of the associated genes in CKO OBs (Fig. 5c). KEGG and GO analysis revealed that these genes are significantly enriched in the Wnt signaling pathway and are involved in skeletal system morphogenesis and development (Fig. 5d, e). Decreased H2AK119ub1 enrichment and corresponding expression patterns in CKO OBs were observed at representative Wnt regulator genes, such as *Wnt10b*, *Fzd10*, with an irrelevant intergenic region as a negative control (Fig. 5f). Collectively, these data suggest that PRC1.1-mediated H2AK119ub1 accounts for the repression of Wnt/β-catenin target genes in OBs.

iBP disassembles PRC1.1 by blocking the interaction between PCGF1 and BCOR

Next, we investigated the possibility of pharmacologic targeting of PRC1.1 and the potential impact on bone formation. To develop specific PRC1.1 inhibitors, we examined the available structural data. We recently identified an electrostatic interaction formed between the linker region of BCOR and the positively charged patch on the F-box and LRRs of KDM2B[39]. However, this interaction surface is rather shallow, lacking a desirable binding pocket for inhibitor design. Here, we focused on the interaction between the BCORL1 PUFD domain and the RAWUL domain of PCGF1, which creates an extended interface for associating with KDM2B and is unique to the PRC1.1[40]. Based on previous studies, a pocket on PCGF1, which packs against two anti-parallel

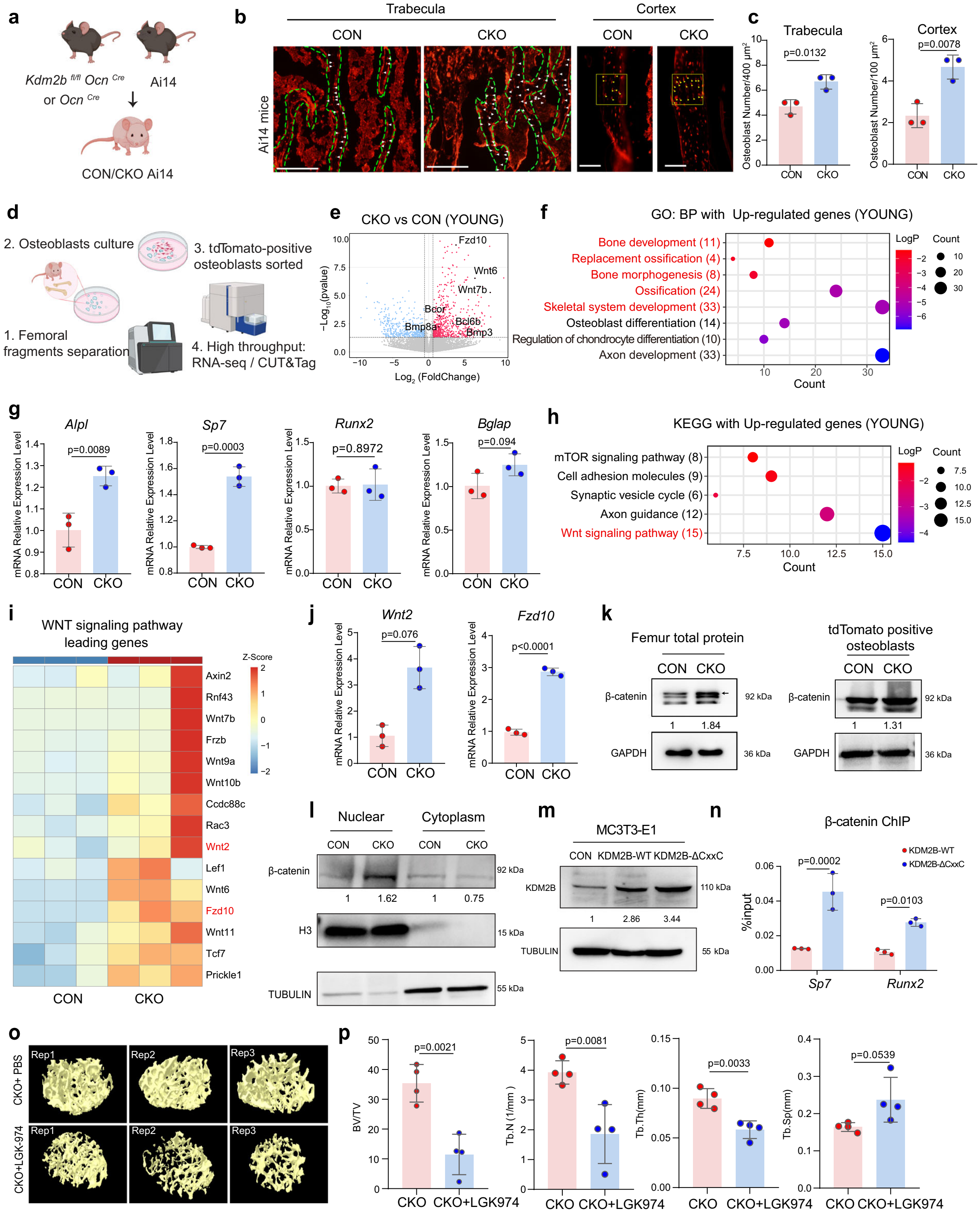

β strands on BCOR (Fig. 6a), is essential for PCGF1-BCOR complex formation[41]. Thereby, inhibitors targeting this pocket would potentially impair PCGF1 binding to BCOR/BCORL1, eventually disrupting the activity of PRC1.1. Based on this analysis, we performed high-throughput virtual screening of 231,000 compounds from ZINC database (Fig. 6b). Based on Docking Scores and visual inspection, 11 hits were selected for activity validation (Supplementary Fig. 4).

To determine the inhibitory potency of these hit compounds on the PCGF1-BCOR interaction in vitro, we conducted a bead-based AlphaScreen assay with recombinant PCGF1^{RAWUL} protein and BCOR^{PUFD}. As the purification of wild type PCGF1^{RAWUL} protein turned out to be rather challenging, eventually we obtained purified PCGF1^{RAWUL} mutant (PCGF1^{RAWUL} L238A/F242A) by mutating hydrophobic residues (L238 and F242) on the surface. In the structure of PCGF1^{RAWUL}/BCOR^{PUFD} complex, these two residues are away from the predicted inhibitor binding pocket (Supplementary Fig. 5), and are surrounding the Leu cage of BCOR^{PUFD} that is less important for the complex formation[41]. AlphaScreen assay showed that, among these selected compounds, Compound **1, 6, 8, 9** exhibited more than 50% inhibition rate for the interaction between PCGF1^{RAWUL} L238A/F242A

Fig. 4 | KDM2B inactivation enhances OB functions through the activation Wnt signaling. **a** Schematic of tdTomato-positive mouse generation. **b** Fluorescent images of trabecular and cortical bone sections from tdTomato mice. White triangles highlight Tomato-positive OBs in the trabecular region (green dashed line, ~400 μm²), while yellow triangles indicate OBs in the cortical region (yellow box, ~100 μm²). **c** Quantification of tdTomato-positive cells in periosteum of trabecula and cortex bone ($n = 3$ mice per genotype). **d** Workflow for isolation, sorting and analysis of tdTomato-positive OBs. **e** Volcano plot of DEGs in OBs isolated from 3-months-old mice ($n = 3$ CON and $n = 3$ CKO). Upregulated genes are labeled in red and downregulated genes in blue (Wald test, $p < 0.05$; |Foldchange| >1.5) OBs were collected after 14 days of culture by removing the bone fragments. **f** and **h** GO enrichment analysis for biological processes and KEGG enrichment analysis in upDEGs (CKO vs CON (YOUNG), Fisher's exact test, $p < 0.05$). Number of genes and statistical significance are shown. **g** and **j** RT-qPCR analysis of representative genes in CKO and control OBs. **i** The heatmap showing the levels of leading genes in Wnt/β-catenin signaling pathway. Gene expression levels are shown as relative *Z*-Scores between two groups. **k** WB analysis of β-catenin levels in total protein lysates of femur tissue and tdTomato-positive OBs of control and CKO mice. GAPDH was used as loading control. **l** WB analysis of cytoplasmic and nuclear β-catenin in tdTomato-positive OBs from control and CKO mice. TUBULIN and H3 were used as fraction-specific controls. **m** WB analysis of KDM2B levels in KDM2B-WT and KDM2B-CxxC deletion mutant overexpressing MC3T3-E1 cells. **n** ChIP-qPCR analysis comparing β-catenin enrichment at target genes in differentiated MC3T3-E1 cells ($n = 3$/group). **o** Representative images of 3D reconstruction of trabecula bone from CKO mice treated with PBS or LGK974 for 1 month. **p** μCT analysis of trabecular parameters ($n = 4$ mice/group). Statistical significance was assessed using Student's *t* tests, two-tailed, in (**c**, **g**, **j**, **p**), error bars are presented as mean values ± SD. Statistical significance was assessed using Two-Way ANOVA, two-tailed, in (**n**), error bars are presented as mean values ± SD. Scale bar, 100 μm. CON: *Ocn* ^{Cre} *td-Tomato*, CKO: *Kdm2b*$^{fl/fl}$ *Ocn* ^{Cre} *td-Tomato* in (**b**–**i**, **o**, **p**); CON: empty vector in (**m**). **a** and **d** created with Biorender (https://biorender.com/w07p252, https://biorender.com/p69f867). Source data of (**c**, **g**, **j**, **k**, **l**, **m**, **n**, **p**) are provided as a Source Data file.

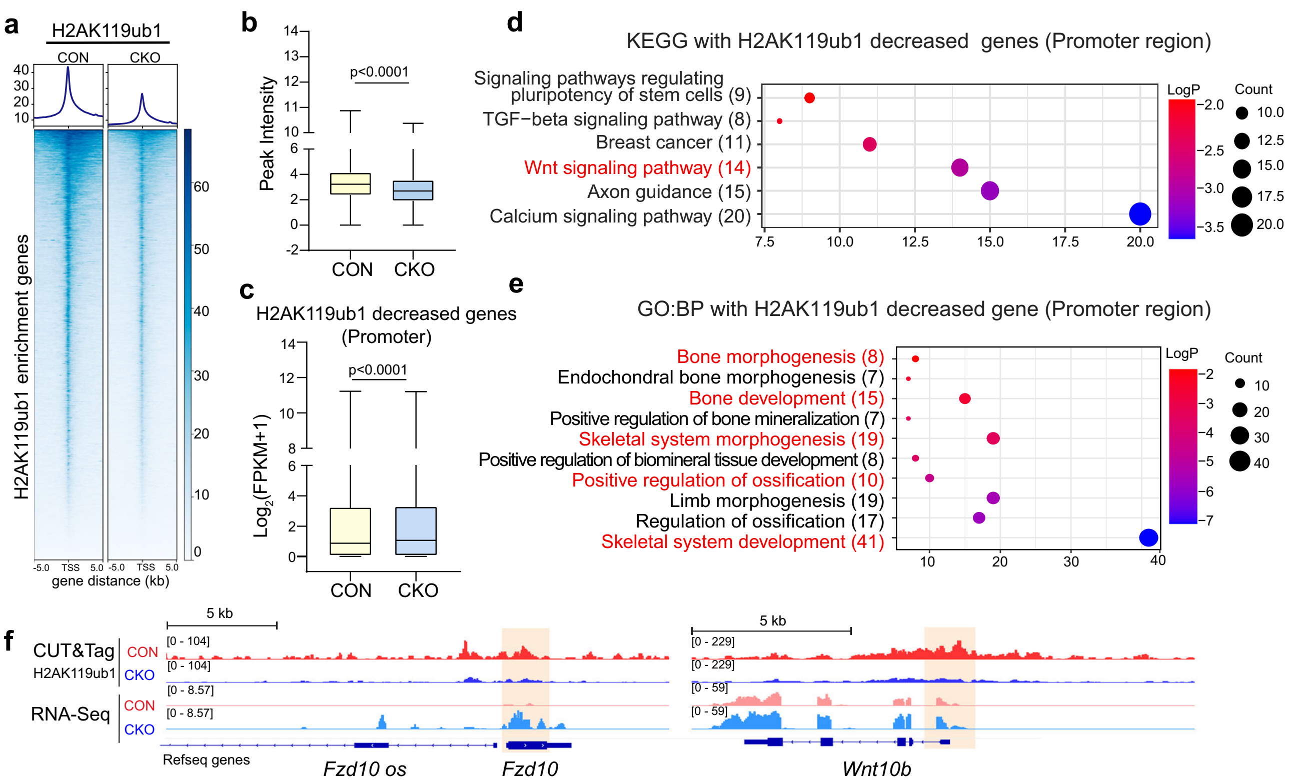

Fig. 5 | Derepression of the Wnt/β-catenin target genes in KDM2B-inactive OBs is associated with reduced H2AK119ub1 enrichment. **a** Heatmaps represent the enrichment for H2AK119ub1 in chromatin of CON and CKO mice around the TSS (± 5 Kb) of H2AK119ub1 target genes. (n = 2 per group). Colors represent CUT&Tag RPM, and rows are ranked by CUT&Tag signals in CON. **b** Box plot showing peak intensity of CUT&Tag reads for H2AK119ub described in panel (**a**). (Wilcoxon matched-pairs signed rank test, two tailed, $p < 0.0001$) **c** Quantification of $\log_2$-transformed fold change of expression levels of H2AK119ub1 decreased genes (CKO vs CON, $n = 759$) in promoter region of OBs ($n = 3$ per group, Wilcoxon matched-pairs signed rank test, two tailed, $p < 0.0001$). The box plots in (**b**) and (**c**) indicate the median (centre line), the third and first quartiles (box limits) and 1.5 × IQR above and below the box (whiskers). (**d**, **e**) KEGG enrichment analysis and GO enrichment analysis for biological processes of genes described in (**c**), ($n = 763$, Fisher's exact test, $p < 0.05$). Number of genes and statistical significance are shown. (**f**) The IGV view of decreased H2AK119ub1 enrichment at representative Wnt/β-catenin target genes and increased gene expression levels in control and CKO OBs. An intergenic region serves as a negative control. CON: *Ocn* ^{Cre} *td-Tomato* CKO: *Kdm2b*$^{fl/fl}$ *Ocn* ^{Cre} *td-Tomato*. Source data of (**b**, **c**) are provided as a Source Data file.

and BCOR^{PUFD}, with Compound 8 (C8) achieving an inhibition rate about 95% at concentration of 200 μM (Fig. 6c).

Meanwhile, we assessed the cellular efficacy of these candidate compounds using a Split-GFP system (Fig. 6b), which relies on the self-association of GFP10 and GFP11 with GFP1-9 to reconstitute a functional GFP upon interaction of the fused proteins[42]. We fused PCGF1 and BCOR into plasmids with GFP1-10 and GFP11 fragments, respectively, and co-transfected the plasmids into 293 T cells (Fig. 6d). High-content imaging and analysis revealed that among the compounds tested, C6 and C8 significantly downregulated GFP fluorescence intensity, with C8 exhibiting the most potent efficacy (Supplementary Fig. 6a and e). Based on these in vitro and intracellular screenings, we selected C8 as the optimal candidate and named it as "iBP", the inhibitor of BCOR-PCGF1 (Fig. 6f and Supplementary Fig. 6b). The IC50 of iBP, as determined by AlphaScreen, was 12.21 ± 0.88 μM (Fig. 6g). In addition, affinity measurements revealed

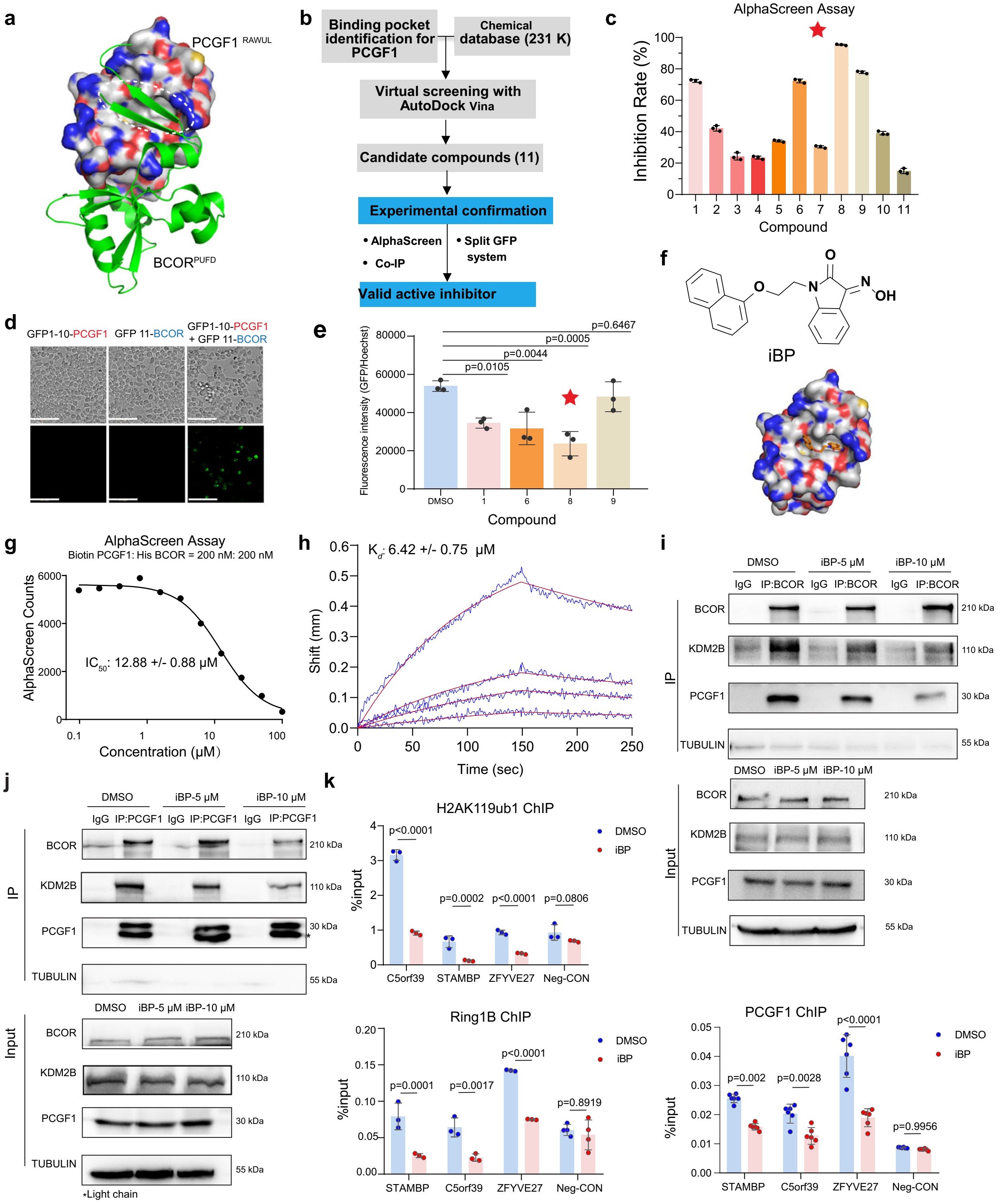

that iBP bound to PCGF1^{RAWUL} L238A/F242A with a dissociation constant (*Kd*) of 6.42 ± 0.75 μM (Fig. 6h).

High-performance liquid chromatography (HPLC) analysis showed that 92.2% and 86.9% of iBP remained after 12 and 24 h (hrs) respectively in cell culture media, indicating iBP's inherent stability (Supplementary Fig. 6c). According to the luminescence cell viability assay in 293 cells, the IC50 of iBP was 42.91 μM (Supplementary Fig. 6d). To determine a safe and effective concentration of iBP, we conducted Co-Immunoprecipitation (Co-IP) assays in 293 T cells. Titrating iBP to 5 and 10 μM, we found that 10 μM was sufficient to inhibit the interaction between PCGF1 and BCOR, without disrupting PRC2 or PRC1.4 integrity (Fig. 6i, j and Supplementary Fig. 7a, b). WB analysis showed a reduction of total H2AK119ub1 levels in 293 T cells following treatment with 10 μM iBP (Supplementary Fig. 7c). ChIP-qPCR analysis further demonstrated a significant reduction in the enrichment of PCGF1, RING1B and H2AK119ub1 levels specifically at target promoter regions following iBP treatment (Fig. 6k). These findings confirm iBP as a potent and selective PRC1.1 inhibitor.

Fig. 6 | Screening and validation of specific PRC1.1 inhibitors. a Structural model of the binding interface between PCGF1-BCOR complex (PDB: 4HPL). The RAWUL domain of PCGF1 is shown as a surface (carbon in white, oxygen in red, nitrogen in blue, sulfur in yellow), while the PUFD domain of BCOR is depicted as a green cartoon. **b** Flowchart of screening and verification of PRC1.1 inhibitors. **c** AlphaScreen assay to show the inhibition of PCGF1^{RAWUL} L238/F242 interaction with BCOR^{PUFD} by selected compounds. **d** Split-GFP system construction. Representative images of each group of transfected 293 T cells are shown. Scale bar, 100 µm. **e** Quantification of GFP/Hoechst fluorescence intensity in 293 T cells co-transfected with GFP1-10-PCGF1 and GFP11-BCOR, subsequent to treatment with candidate inhibitors. Statistical significance was assessed using One-Way ANOVA, two-tailed, error bars are presented as mean values ± SD ($n = 3$ per group). **f** Chemical structure of iBP (Left). Docking model of PCGF1^{RAWUL} (surface) and iBP (orange stick). **g** AlphaScreen determination of iBP's IC50 value for inhibiting the interaction between PCGF1^{RAWUL} L238A/F242A and BCOR^{PUFD}. **h** Biolayer interferometry (BLI) analysis of iBP binding to PCGF1^{RAWUL} L238A/F242A. Representative data and 1:1 binding model fit shown as blue and red lines, respectively. **i**, **j** Co-IP assay examining how iBP treatment at various concentrations affects the interaction between PCGF1 and BCOR. **k** ChIP-qPCR analysis comparing H2AK119ub1, PCGF1 and RING1B enrichment at PRC1-target promoters and non-targeted gene bodies as control in control and iBP-treated 293 T cells. Statistical significance was assessed using Two-Way ANOVA, two-tailed, error bars are presented as mean values ± SD ($n = 3 \sim 6$ per group). Source data of (**e**, **g**–**k**) are provided as a Source Data file.

iBP treatment enhances OB functions and reverses bone loss in OVX models

To delineate the functional impact of iBP treatment on aged OBs, we conducted RNA-seq analysis. Strikingly, 1786 genes upregulated in aged OBs exhibited significant enrichment in osteogenic morphogenesis, skeletal development, and Wnt/β-catenin signaling pathways (Fig. 7a, b). Notably, 386 genes downregulated during aging showed marked upregulation in both CKO and iBP-treated aged OBs compared to age-matched controls (Fig. 7c). These findings collectively demonstrate that genetic ablation of KDM2B or pharmacological inactivation of PRC1.1 rescues the transcriptional signature of bone aging.

We also tested iBP's effects on osteogenic differentiation in MC3T3-E1 cells. After 14 days in osteogenic medium (OM), we observed a significant upregulation in the expression of osteogenic marker genes and Wnt/β-catenin target genes, which was further enhanced by iBP treatment (Supplementary Fig. 7d, e). Additionally, transfecting MC3T3-E1 cells with the TOP-FLASH reporter plasmid, containing six TCF-binding motifs upstream of a luciferase gene, revealed that iBP treatment significantly activated the Wnt reporter. This activation was reversed by LGK974 (Supplementary Fig. 7f). These data demonstrate that iBP treatment enhances OB functions as well as KDM2B ablation.

To evaluate the drug's toxicity and metabolic profile in vivo, pharmacokinetic (PK) studies were conducted. Following an intraperitoneal administration of 20 mg/kg iBP to C57/BL6 mice, the maximum concentration (C_{max}) of iBP reached 3209 ng/mL (9.66 µM) at 0.083 h (T_{max}) (Supplementary Fig. 8a), approaching the effective concentration of 10 µM noted in 293 T cells. Moreover, iBP exhibited acceptable plasma exposure ($AUC^{0\text{-}t}$, 1973 h × ng/mL) and half-life (T1/2, 1.05 h). Importantly, iBP was well tolerated by the tested mice, indicating its suitability for in vivo efficacy studies. Therefore, a 20 mg/kg dose was selected for further experiments.

iBP was administered intraperitoneally to OVX mice for one month (20 mg/kg daily). During this period, OVX mice exhibited weight gain compared to the control sham group, which was modestly restricted by iBP treatment (Supplementary Fig. 8b). Histological examination of heart, liver, spleen, lung, and kidney tissues showed no apparent abnormalities (Supplementary Fig. 8c). Bone metrology analysis following µCT scanning revealed that iBP treatment markedly reversed the loss of trabecular bone in OVX mice, as evidenced by the recovery of BV/TV, Tb.Th, and Tb.N, with no alterations in Tb.Sp (Fig. 7d, e). Increased trabecular bone was also confirmed by sagittal plane H&E staining (Fig. 7f). Immunohistochemistry (IHC) assay demonstrated that the expression levels of WNT2, WNT3a and β-catenin were increased in iBP-treated femur (Fig. 7g). These data indicate that iBP treatment effectively activates Wnt signaling and prevents osteoporosis.

iBP treatment accelerates bone healing

Then we continued to examine whether iBP could foster bone repair in bone trauma models. To enhance local repair efficiency, we formulated an iBP-loaded hydrogel for targeted and controlled drug delivery. F127, a thermosensitive hydrogel known for its temperature responsiveness, biodegradability, and excellent biocompatibility[43], was selected for this purpose. It solidifies at room temperature (RT) (25°), as shown in Supplementary Fig. 8d.

Analysis of particle size and surface charge revealed iBP particles to be around 162 nm in diameter (Fig. 8a and Supplementary Fig. 8e). Scanning electron microscopy showed the hydrogel voids to be approximately 10 µm in diameter (Fig. 8b), implying that the nano-sized iBP would result in an initial burst release. Gelatin, known to reduce the burst release of F127, is clinically utilized for bone wound hemostasis[44,45], making it a promising candidate for iBP delivery. We cut gelatin sponges to a specific size ($2 \times 2 \times 10$ mm^3) (Supplementary Fig. 8f) and injected cold (4 °C) liquid iBP-loaded F127 into them before quickly transferring them to a 37 °C incubator to facilitate solidification within the sponge (Fig. 8c). Based on the UV absorbance spectrum of iBP, which peaks at 300 nm, we established a standard curve (Supplementary Fig. 8g, h) and found that a 20% F127@gelatin sponge loaded with 2 mg/ml iBP exhibited a sustained release over 14 days, with an average drug release concentration of 20 µM (Fig. 8d). Thus, we successfully developed a sustained-release delivery system for iBP.

With this system, we evaluated the healing effects of iBP. Notably, after 14 days of healing, mice that received local iBP treatment exhibited a significantly larger amount of new callus formation compared to mice in the mock or hydrogel-only control groups, as revealed by µCT scanning (Fig. 8e, f). These findings indicate that iBP treatment promotes new bone formation in vivo.

Discussion

Epigenetic regulation plays critical roles in tissue homeostasis, extending beyond lineage differentiation and development. In this study, we provide genetic evidence that KDM2B inactivation in OBs enhances bone homeostasis by derepressing Wnt/β-catenin target genes due to impaired PRC1.1 activity. Based on this finding, we have developed a specific PRC1.1 inhibitor, iBP, which enhances osteogenic functions in mouse models of osteoporosis and acute trauma (Supplementary Fig. 9).

The processes of cell signal transduction and epigenetic regulation are intricately linked in OB differentiation, bone formation, and homeostasis. Current strategies to increase bone density, such as administering Wnt ligands, Vitamin D, Parathyroid Hormone (PTH), or Bone Morphogenetic Proteins (BMPs), rely heavily on extracellular factors[46]. However, the effectiveness of these approaches depends on the systemic or local microenvironment, which influences chromatin states and thus responsiveness to signaling cascades. This underscores the importance of identifying chromatin regulators that shape the chromatin landscape, facilitating osteogenic lineage commitment and bone remodeling.

The biochemistry and epigenomic regulation of PRCs have been well characterized. In stem cells, PRCs are known to preserve their differentiation potential by silencing key developmental genes, keeping them in a poised state ready to respond to signaling cues[15,20,22]. For example, the Wnt10b pathway promotes mesenchymal stem cell

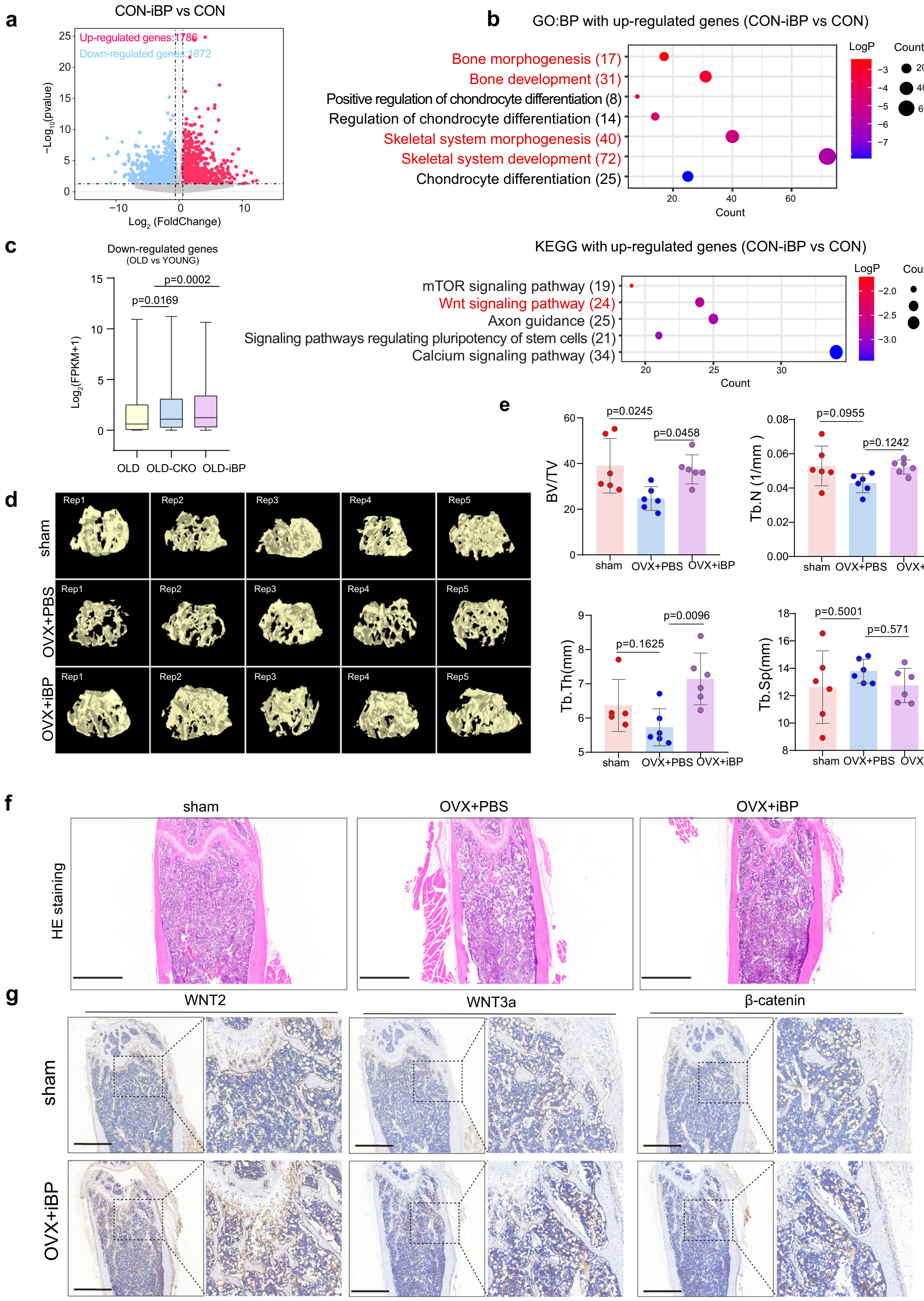

(MSC) differentiation towards OBs[47,48], a process that PRCs restrict. Accordingly, EZH2 inhibition stimulates OB differentiation[32,49]. However, the composition and chromatin binding of PRCs vary dynamically across different developmental stages[22,23,36,50,51], during aging[52,53], disease progression or under drug treatment[54–57]. The context-dependent regulation of PRCs and their functions will be an interesting direction for future research. Our unexpected observation of increased PRC1.1 activity in aging bones raises intriguing questions about potential upstream modulators. While our study delineates the functional consequences of PRC1.1 activation in aged OBs, the molecular triggers driving its enhanced activity remain incompletely resolved. We postulate that unidentified signaling cascades or post-translational modifications of KDM2B-PRC1 components may fine-tune its chromatin-binding affinity or enzymatic robustness in aging contexts.

Fig. 7 | iBP treatment enhances OB functions and reverses bone loss in OVX models. **a** Volcano plot of DEGs in OBs ($n = 3$ CON and $n = 3$ CON-iBP). Upregulated genes are labeled in red and downregulated genes in blue (Wald test, $p < 0.05$; |Fold change| >1.5). The *x*-axis shows the $\log_2$ (fold change) in gene expression between CKO and control OBs, and the *y*-axis shows the statistical significance of the differences. OBs were collected after 14 days of culture by removing bone fragments. **b** GO enrichment analysis for biological processes and KEGG enrichment analysis of upDEGs in (**a**), (CKO-iBP vs CON, $n = 1786$, Fisher's exact test, $p < 0.05$). Number of genes and statistical significance are shown. **c** Boxplots showing $\log_2$-transformed fold change of expression levels of downDEGs in aged OBs (OLD vs YOUNG, $n = 386$) following KDM2B ablation or iBP treatment ($n = 3$ per group, Wilcoxon matched-pairs signed rank test, two tailed, $p < 0.0001$). The boxplots indicate the median (centre line), the third and first quartiles (box limits) and 1.5 × IQR above and below the box (whiskers). **d**, **e** Images of 3D reconstruction of trabecula bone of OVX mice treated with iBP or PBS, with sham group as controls. CT analysis of the distal femur metaphysis. Statistical significance was assessed using One-Way ANOVA, two-tailed, error bars are presented as mean values ± SD, $n = 5$ per group. **f** H&E staining of femur of the designated groups of mice. **g** IHC staining of WNT2, WNT3A and β-catenin in femurs of the designated groups of mice. Scale bar, 1 mm. OVX, Ovariectomy. Source data of (**e**, **f**, **g**) are provided as a Source Data file.

Detailed phenotypic analyses in mouse models reveal that PRC1.1 inactivation not only enhances OB function but also promotes OB differentiation. This increase in OB differentiation is supported by the elevated OB counts in CKO mice and the activation of Wnt/β-catenin and osteogenic genes in PRC1.1-inactive pre-OB cells. Consistently, BCOR deficiency in MSCs enhances osteo-dentinogenic differentiation. BCOR loss-of-function mutations are associated with oculo-facio-cardio-dental (OFCD) syndrome, which includes characteristic dental and neural crest defects[58]. In contrast, the inactivation of PR-DUB complex as evidenced by *Asxl1* deletion causes gain of H2AK119ub1 activity and significant OB dysfunction and bone loss[59]. These evidence highlight a critical role of H2AK119ub1 activity in the epigenetic regulation of OB lineage differentiation and functions. Additionally, KDM2B inactivation also enhances OC activity (Supplementary Figs. 1f, g and 2c, d), suggesting a new equilibrium in which bone formation and resorption are heightened upon PRC1.1 inhibition.

Our transcriptomic and epigenomic analyses indicate that excessive PRC1.1 accumulation raises the activation threshold for Wnt/β-catenin target genes, a crucial regulatory mechanism for bone homeostasis. PRC1.1 inactivation lowers this threshold, enhancing the transcriptional response to Wnt signaling, particularly under bone-loss conditions associated with PRC1.1 gain, such as aging. Additionally, PRC1.1 inhibition may increase chromatin accessibility to various stimuli, indicating that combining PRC1.1 targeting with extracellular osteogenic factors could provide synergistic therapeutic benefits.

Existing PRC1 inhibitors like PRT-4165[60], RB-3[61], etc. target RING1B's E3 ligase activity or the stability of key partner proteins, broadly affecting PRC1 complexes. In contrast, iBP selectively targets PRC1.1, potentially minimizing side effects. In our OVX mouse models, it showed no significant toxicity over one month of treatment. Our study provided the core structure of iBP, which could function as a lead compound for future optimization to improve its bioavailability. Additional long-term studies in aged mice with varying doses are necessary to confirm its safety and efficacy. Beyond bone disease, iBP could offer insights into PRC1.1's role in transcriptional regulation and might be applicable to other conditions, such as PRC1.1-overactive cancers[62,63].

However, our study has some limitations. The factors driving PRC1.1 gain during aging and its occurrence in other pathological conditions are still unknown. Additionally, the detailed regulatory mechanisms by which PRC1.1 influences OB differentiation and OC activity require further elucidation. Moreover, clinical applicability will depend on assessing PRC1.1 expression patterns and relevant epigenomic profiles in human bone deterioration disorders.

In summary, our genetic mouse models and chemical screenings reveal a promising epigenetic therapeutic strategy to increase bone density. iBP may serve as a candidate for treating other conditions characterized by aberrant PRC1.1 function, offering a novel approach to address bone loss and related diseases.

Methods

Mice

All C57BL/6 mice were maintained in specific pathogen-free barrier facilities and housed at 20–22 °C with 12 h:12 h light: dark cycles at 50–60% humidity, animals were used in accordance with protocols approved by the institutional animal care and user committee (Approval No. TMUaMEC 2020008) at the Tianjin Medical University (SYXK(JIN)−2020-0010). The details of mice age and sex are provided in the main text and figure legends. *Kdm2b$^{fl/fl}$* mice were reported previously[18]. *Ocn-Cre* mice were purchased from Cyagen. *Ai14(Rosa-CAG-LSL-tdTomato)* mice were a gift from Dr. Zhiyong Liu, Institute of Neuroscience, CAS. *Kdm2b$^{fl/fl}$* mice were cross-bred with *Ocn-Cre* mice to specifically delete KDM2B-CxxC domain OBs (*Kdm2b$^{fl/fl}$ Ocn-Cre*). The genotyping primers are listed in Supplementary Table 1. Age- and sex-matched littermates *Ocn-Cre* mice were used as control.

Isolation and culture of OBs

To isolate OBs, femurs from 3-month-old and 18-month-old C57BL/6 mice were cleaned of surrounding tissue. After the bone marrow was flushed out with phosphate-buffered saline (PBS), the bone tissue was cut into small pieces. These bone fragments were then digested overnight at 37 °C using Type II collagenase (C8150, Solarbio) and subsequently cultured in α-MEM medium supplemented with 10% FBS (LONSERA, Suzhou Shuangru Biotechnology) and 1% penicillin-streptomycin (P/S) (Sigma) in a humidified incubator at 37 °C with 5% CO_2. Adherent OBs were collected after 14 days of culture by removing the bone fragments[64]. For tdTomato-reporter mice, OBs were processed similarly and subsequently sorted using flow cytometry based on tdTomato expression, which was used as a marker for OBs.

Culture and osteogenic induction of MC3T3-E1 cells

MC3T3-E1 cells are grown in Dulbecco's Modified Eagle's Medium (DMEM, Gibco) medium (GM) supplemented with 10% FBS, 10 mM HEPES (Sigma), 1% P/S. The cells were maintained in a humidified incubator at 37 °C with an atmosphere of 5% CO_2. The culture medium was changed every 2 and 3 days to ensure cell growth and proper maintenance. For osteogenic differentiation, the MC3T3-E1 cells were induced with an osteogenic medium (OM), which consists of 10% FBS in DMEM, 50 µM ascorbic acid, 10 mM β-glycerol phosphate, and 100 nM dexamethasone.

WB

For the extraction of total proteins from OBs, cells were lysed in RIPA buffer supplemented with a phosphatase and protease inhibitor cocktail (PIC, HY-K0010, MCE). For bone tissues, femurs were isolated from the surrounding soft tissues, and the mid-shaft portions were carefully dissected and ground into a fine powder under liquid nitrogen and a mortar and pestle. These powders were then lysed in RIPA buffer containing the same inhibitor cocktail for 30 min (min) at 4 °C. After centrifugation at 12,000 × *g* for 15 min at 4 °C to remove cellular debris, the supernatant containing the total protein extract was collected, and the proteins were denatured and separated by SDS-PAGE on a 10–12% polyacrylamide gel, depending on the protein size. The resolved proteins were transferred onto polyvinylidene fluoride (PVDF) membranes at 300 mA for 2 h. The membranes were blocked with 5% non-fat dry milk in Tris-buffered saline with 0.1% Tween-20

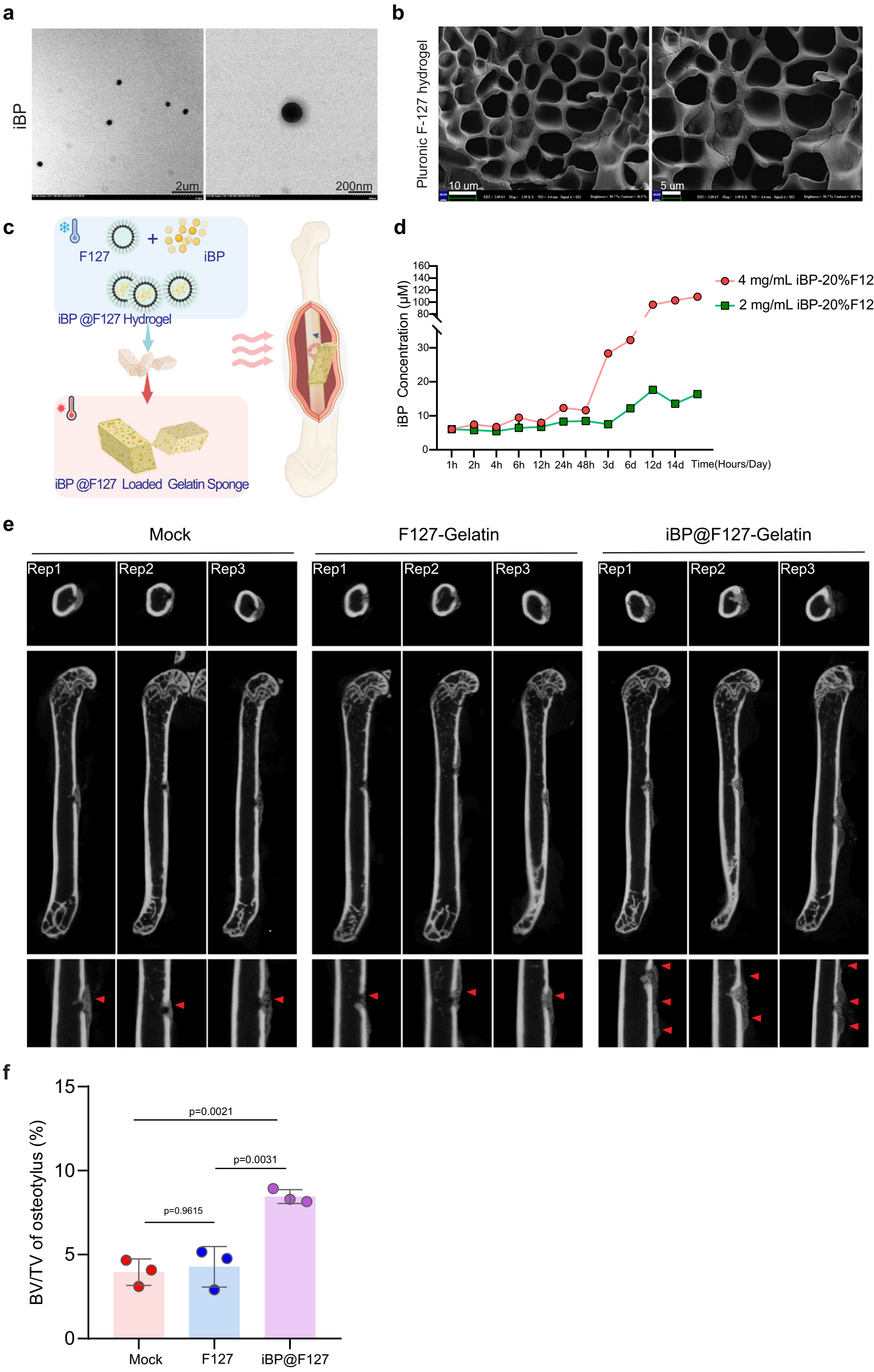

Fig. 8 | iBP treatment accelerates bone healing. **a** Images obtained by transmission scanning microscope of iBP. **b** Images of scanning electron microscope of F127. **c** Schematic diagram of construction of iBP loaded gelatin sponge -F127 hydrogel. **d** Statistical analysis of sustained release efficiency of iBP for 14 days. **e** Representative images of scanned sections and sagittal plane views of femur defects in the designated treatment groups for two weeks. Red triangles indicate the new callus at the sites of circular bone defect. **f** BV/TV quantification of the osteotylus in (**e**). Statistical significance was assessed using One-Way ANOVA, two-tailed, error bars are presented as mean values ± SD, *n* = 3 per group, Mock: A model representing femur defects, F127-Gelatin: femur defects area treated with F127-Gelatin for two weeks, iBP@F127-Gelatin: femur defects area treated with iBP@F127-Gelatin for two weeks. **c** created with Biorender (https://biorender.com/j89n671). Source data of (**a**, **b**, **d**, **f**) are provided as a Source Data file.

(TBST) for 1 h at RT to reduce non-specific binding. After blocking, membranes were then probed with specific primary antibodies which are listed in Supplementary Table 2. Following incubation with appropriate secondary antibodies, the membranes were washed three times for 5 min each with TBST. The blots were visualized using the NcmECL High Reagent (P2300, New Cell & Molecular Biotech) and captured with a Uvitec Cambridge Imaging System. The protein bands were quantified using ImageJ software by normalizing to an internal control.

RNA-Seq

The library preparation and sequencing were conducted by Novogene, using an Illumina Novaseq platform to generate 150 bp paired-end reads. The raw sequencing data were first cleaned to remove low-quality reads. Clean reads were aligned to the mm39 reference genome with Hisat2 (v2.2.1), and Samtools (v1.19) was used to convert sam files to bam files. Deeptools (v3.5.4) was employed to generate bigwig files, with visualization done via Integrative Genomics Viewer. Gene counts were calculated by Stringtie (v2.2.1), and differential expression analysis was performed using the R package DESeq2 (v1.34.0). Genes were considered significantly different if they met the criteria of $P < 0.05$ and $|\log_2\text{FoldChange}| > 0.585$. Volcano plots and heatmaps were generated with R packages ggplot2 (v3.4.3) and pheatmap (v1.0.12). Pathway enrichment analysis was performed using Metascape, and selected pathways were visualized with R packages ggplot2 (v3.4.3)[65].

CUT&Tag

CUT&Tag assay was performed using the Hyperactive Universal CUT&Tag Assay Kit (TD904, Vazyme) as previously described[36]. Briefly, 100,000 cells were harvested, washed, and resuspended in wash buffer before incubation with pre-activated concanavalin A beads. Primary anti-H2AK119ub1 antibody (1:1000, 8240S, CST) and secondary antibodies were added sequentially, followed by incubation with Dig-wash buffer and pA/G-Tnp Pro was added to initiate tagmentation. Once tagmentation was complete, DNA was extracted from the beads, and an equal amount of *E. coli* DNA was added as a spike-in control. After DNA extraction and PCR amplification, sequencing was performed on an Illumina Novaseq6000 platform (Annoroad Gene Technology, Beijing). Raw data underwent quality evaluation with Fastqc (v0.12.1) and Multiqc (v1.19). Adapters were removed with Trim-galore (v0.6.10). Clean reads were aligned to the mm39 reference genome and λDNA (TD904, Vazyme), normalized based on scale-factor, and duplicates removed with Sambamba (v1.0). Peak calling was conducted with Macs2 (v2.2.9.1), and bigwig files were generated with Deeptools (v3.5.4). Peaks were annotated with R packages ChIPseeker (v1.30.3), and pathway enrichment analysis was performed using Metascape (https://metascape.org/gp/index.html). Visualization of selected pathway were generated by R packages ggplot2 (v3.4.3)[65].

μCT

To observe and evaluate bone microstructure, μCT analysis was performed. Briefly, femurs were harvested from mice, fixed overnight in 4% paraformaldehyde (PFA), and scanned with an isotropic voxel size of 8 μm and a peak tube voltage of 55 kV and current of 100 μA (SKYSCAN 1276; Bruker). Three-dimensional images were reconstructed and regions of interest (ROI) were analyzed using NReconServer, CTAn, and CTvox softwares (GE). Trabecular bone parameters were measured from 100 consecutive slices of the distal metaphysis, devoid of epiphyseal structures.

Calcein double labeling and three-point bending test

For calcein double labeling, mice were injected with calcein at 10 mg/kg on day 13 and day 3 prior to femur harvest. Femurs were fixed, embedded in methylmethacrylate, and sectioned at 5 μm. Images were acquired using a fluorescence confocal microscope, and bone formation rates (BFR/BS and BFR/TV) were calculated from fluorochrome double labels at periosteal and endocortical surfaces using OsteoMeasure software. The three-point bending test was conducted on fresh femurs to assess structural and material strength using an Instron electromechanical tester (Instron 3367). Load-displacement curves were recorded until fracture, and the maximum force at failure was calculated.

H&E staining, TRAP staining and IHC

Samples including femurs, heart, liver, spleen, lung, and kidney were collected and sectioned at 5 μm for H&E staining. Paraffin sections were dewaxed, stained with hematoxylin and eosin, dehydrated, and sealed[66]. For IHC, slides were stained with specific antibodies which are listed in Supplementary Table 2. Sections were deparaffinized, rehydrated, and antigen retrieval was performed with 3% hydrogen peroxide. After blocking with 3% BSA, primary and secondary antibodies were applied, and DAB substrate was used to develop signals. For TRAP staining, sections were deparaffinized, rehydrated, and stained with a TRAP staining kit (G1050, Servicebio). Images were scanned at ×100 magnification (Pannoramic 250 FLASH, 3DHISTECH), and OB/OC counts were performed using ImageJ software.

IF staining

Femurs were fixed in 4% PFA and decalcified in EDTA solution before embedding in OCT compound and sectioning at 8 μm. Sections were stained with an anti-β-Catenin antibody. For OBs, cells were fixed in 4% PFA, permeabilized with 0.2% Triton X-100, and blocked with 3% BSA[67]. Sections were then incubated with primary antibodies: RUNX2 (1:100, 12556S, Cell Signaling Technology), ALP (1:100, AB_2838191, Affinity Biosciences Cat# DF6225) and the sections were incubated with corresponding secondary antibodies conjugated to fluorescent dyes. DAPI were used to stain the nuclei. Images were captured using a fluorescence microscope.

ChIP-PCR analysis

Cells (1×10^6) were used for each immunoprecipitation following a previously described protocol[36]. In brief, cells were crosslinked with 1% formaldehyde at RT in medium for 10 min, after which glycine was added to a final concentration of 0.125 M to quench the crosslinking and incubate at RT for 5 min. Cells were washed twice with PBS and lysed with SDS buffer (100 mM NaCl, 50 mM pH 8.1 Tris-HCl, 5 mM pH 8.0 EDTA, 0.02% NaN_3, 0.5% SDS, PIC) at RT for 5 min. Cell lysates were harvested, and samples were thawed in a water bath to ensure complete dissolution of SDS. After centrifugation at 4 °C 1200 × *g* for 6 min, the supernatant was discarded and 1 mL of prechilled IP buffer (a mixture of SDS buffer and Triton Dilution Buffer in a 2:1 ratio, supplemented with PIC) was added. Samples were then sonicated to produce 0.2–0.5 Kb DNA fragments, centrifuge sonicated chromatin 13,000 × *g* for 30 min.

Equal amount of lysates was taken, and the volume was adjusted to 1 mL with IP buffer. Primary antibodies as listed in Supplementary Table 2 were added for IP overnight at 4 °C with rotation. Protein A/G beads were then added and incubated on a rotating wheel at 4 °C for 2 h. Beads were washed once with 1 mL of 150 mM wash buffer (containing 1% TritonX-100, 0.1% SDS, 150 mM NaCl, 2 mM EDTA pH 8.0, 20 mM Tris-HCl pH 8.0), and then twice with 500 mM wash buffer (containing 1% TritonX-100, 0.1% SDS, 500 mM NaCl, 2 mM EDTA pH 8.0, 20 mM Tris-HCl pH 8.0). Finally, 120 μL of de-crosslinking buffer was added to both input and IP samples and incubated at 65 °C overnight at 1200 × *g* to elute the complexes from beads. QIAGEN PCR purification kit was used for ChIP-DNA purification, and the samples were quantified by real-time PCR using primers listed in Supplementary Table 1.

RNA isolation and qRT-PCR

Total RNA was isolated using kit (M050, New Cell & Molecular Biotech) following the manufacturers' instruction and reverse transcribed using HiScript III All-in-one RT SuperMix (R333-01, Vazyme). The resulting cDNA was used for PCR which was conducted in 10-μl reactions using SYBR Green Master Mix (Q711-03, Vazyme) with the LightCycler480 system. The relative expression of target genes was calculated using method of $2^{-\Delta\Delta CT}$ and calculated after normalization to the expression levels of rp0 in each sample. Primers used in qRT-PCR was listed in Supplementary Table 1.

Dual luciferase assay

To detect relative luciferase activity of TOP reporter, 3T3-E1 cells were co-transfected with 100 ng TOP-FLASH plasmid harboring six TCF-binding motifs (Millipore), and 2 ng of the renilla luciferase control vector pGL4.74 (Promega). Following a 7-day incubation in OM, cell lysates were prepared using the lysis buffer from the TransDetect® Double-Luciferase Reporter Assay Kit (FR201, TransGen Biotech, China). Luciferase activity was subsequently quantified using a GloMax 20/20 luminometer (Promega)[68].

High-throughput screening with AutoDock Vina

Compounds from ZINC database were subject to docking by using AutoDock Vina. Structure of PCGF1^{RAWUL} was taken from crystal structure of PCGF1^{RAWUL} –BCOR^{PUFD} complex (PDB code 4HPL). pdbqt file of PCGF1^{RAWUL} was generated usinig MGL Tools. PCGF1^{RAWUL} protein was prepared by adding hydrogen atoms and Kolloman charges. The pocket on PCGF1^{RAWUL}, that packs against two anti-parallel β strands on BCOR^{PUFD}, was defined as a potential ligand binding site. The grid box was generated using grid-box option from MGL Tools. Each ligand was docked using exhaustiveness value of 16, and energy_range value of 0.1.

Protein purification

The cDNA encoding PCGF1^{RAWUL} L238A/F242A mutant (amino acids 166-255) was cloned into pGEX 6P-1 vector with N-terminal GST and hexa-histidine tag followed by PreScission Protease cleavage site. The cDNA encoding BCOR^{PUFD} (residues 1580-1696) was cloned into pET-28a vector with N-terminal hexa-histidine tag. Both PCGF1^{RAWUL} L238A/F242A mutant and BCOR^{PUFD} were expressed in *E. coli* BL21 (DE3) strain, respectively. Cultures were grown at 37 °C to OD_{600} of 0.6–0.8 before induction with 0.5 mM IPTG, and incubated for an additional 20 hrs at 16 °C to promote protein expression.

For the purification of PCGF1^{RAWUL} L238A/F242A mutant, cells were harvested and resuspended in lysis buffer (20 mM Tris pH 8.0, 1 M NaCl, 7 mM β-mercaptoethanol, 5% glycerol). The recombinant protein was purified using Ni^{2+} affinity chromatography, followed by cleavage of the GST and His tags with PreScission Protease. The mutant PCGF1 ^{RAWUL} was further refined by additional Ni^{2+} affinity chromatography and gel filtration on a Superdex 75 (16/60) column pre-equilibrated with a buffer comprising 20 mM HEPES pH 7.5, 150 mM NaCl, 10% glycerol, and 0.5 mM TCEP. For the purification of His-BCOR^{PUFD}, cells were harvested and resuspended in lysis buffer (20 mM Tris pH 8.0, 300 mM NaCl, 7 mM β-mercaptoethanol, 5% glycerol). His-BCOR^{PUFD} was purified using a Ni^{2+} affinity column with standard protocol, and followed by gel filtration on a Superdex 75 (16/60) column pre-equilibrated with a buffer comprising 20 mM HEPES pH 7.5, 150 mM NaCl, 10% glycerol, and 0.5 mM TCEP.

AlphaScreen assay

The PCGF1^{RAWUL} L238A/F242A mutant was biotinylated using Biotinylation kit (G-MM-IGT, Genemore, Shanghai, China) according to manufacture's instructions. A concentration of 200 nM biotinylated PCGF1^{RAWUL} L238A/F242A mutant was mixed with inhibitor at indicated concentration in the buffer containing 50 mM MOPS pH 7.4, 0.05 mM CHAPS, 50 mM NaF and 0.1 mg/mL BSA, and incubated for 15 min at room temperature. After adding 7.5 μg/mL Nickerl chelate beads, 7.5 μg/mL Streptavidin beads and 200 nM His-BCOR, the mixture was then incubated for additional 1.5 h at 20 °C. Finally, the mixture was transferred to 384-well plate and analyzed by a EnVision 2105 (PerkinElmer). Data were plotted using GraphPad Prism software.

Biolayer interferometry assay (BLI)

Biolayer interferometry equipment (Gator Bio) was used to determine the binding affinity between iBP and the PCGF1^{RAWUL} L238A/F242A mutant. Biotinylated PCGF1^{RAWUL} L238A/F242A at concentration of 50 μg/mL was immobilized on a SA XT biosensor. To remove non-specific bound, the biosensors were washed with assay buffer (50 mM MOPS pH 7.4, 0.05 mM CHAPS, 50 mM NaF, 0.1 mg/mL BSA and 0.5% DMSO). After obtaining a baseline reading in assay buffer, the biosensors were dipped into reference well or wells containing the various concentration of iBP for 5 min. Then, the biosensors were washed with assay buffer for 2 min. Binding kinetics were analyzed using 1:1 binding model with on-board software. Data were plotted using GraphPad Prism software.

Stability assay of iBP

iBP (Vitas-M, STL373868) stability (400 μM) was assessed using HPLC following incubation in DMEM supplemented with 10% FBS at 37 °C for 0, 12, or 24 h. To facilitate the precipitation of proteins from FBS, the incubation mixture was diluted with a fourfold volume of acetonitrile and centrifuged. The resulting supernatant was then subjected to HPLC analysis to determine the remaining iBP concentration.

HPLC

HPLC analysis for iBP was conducted using a Shimadzu LC-20AT system equipped with an SPD-20A UV–VIS detector. The chromatographic separation was achieved on a 4.6 × 150 mm Agilent Eclipse XDB-C18 5 μm column. The mobile phase consisted of solvent A (water with 0.1% trifluoroacetic acid) and solvent B (acetonitrile) at a flow rate of 1.0 mL/min. The gradient elution program was as follows: 10% B (0–2 min), 10–100% B (2–16 min), 100% B (16–18 min), 100–80 % B (18–19 min) and 80% B (19–20 min).

Mouse PK Study

A standard pharmacokinetic study was conducted on iBP using C57BL/6J mice ($n = 3$). The intraperitoneal injection formulation consisted of a 4 mg/mL solution of iBP prepared with a ratio of 10% DMSO, 40% PEG300, 5% Tween 80, and 45% Saline. The mice were administered iBP intraperitoneally at a dosage of 20 mg/kg, and plasma samples were collected at intervals of 5 min, 15 min, 30 min, 1, 2, 4, 8, and 24 h post-injection. The harvested supernatant was diluted with water at a 1:2 ratio, and 2 μL of the diluted supernatant was subjected to LC/MS/MS for quantitative analysis.

Scanning electron microscope (SEM) and transmission electron microscopy (TEM)

The surface structure of the F127 hydrogel (20% W/V) was examined using SEM[69]. Briefly, samples were freeze-dried using an LGJ-12A freeze dryer (China), gold-coated, and imaged with a Zeiss Gemini 300 SEM. The morphology of iBP was observed under a HT7700 TEM (Hitachi High-Tech, Tokyo, Japan). The size and size distribution of iBP particles were further analyzed using a Zetasizer Nano ZS automatic particle size detector (Malvern, UK).

In vitro drug release assay

The release profile of iBP from the F127 hydrogel-gelatin sponge was assessed using a dialysis membrane with a molecular weight cut-off of 3500 Da. Sponges loaded with either 2 mg/mL (100 μL) or 4 mg/mL

(100 µL) of iBP (measuring $2 \times 2 \times 10$ mm^3) were placed in 100 mL of PBS at 37 °C with continuous stirring at 100 × *g*. At each time point, 1 mL of the solution was removed and replaced with 1 mL of PBS to maintain a constant volume. The concentration of iBP in the solution was determined using a standard curve established at OD_{300} nm, recorded with a U-3310 spectrophotometer (Hitachi High-Tech, Tokyo, Japan).

Mouse model construction and In vivo drug administration

For establishing OVX models, mice were randomly assigned to either the OVX or Sham group. Under isoflurane inhalation anesthesia, a lateral dorsal skin incision was made to expose the ovaries. In the OVX group, the ovaries were removed after ligating with bilateral sutures, while in the Sham group, the ovaries were exposed but not removed. Penicillin was administered postoperatively to prevent infection, and the muscle and skin incisions were closed.

To evaluate the therapeutic efficacy of iBP in countering bone loss, 3-month-old virgin female mice were subjected to either ovariectomy or sham surgery ($n = 4$ per group). A subset of ovariectomized mice received daily intraperitoneal injections of iBP at a dose of 20 mg/kg, starting two days post-surgery and continuing for four weeks. A comparative group of ovariectomized mice received PBS injections under the same conditions.

To evaluate the pharmacological effect of iBP on bone healing, a unilateral circular bone defect was created in the right femur of CON and CKO mice. Using a low-speed dental drill with a 1 mm diameter bit, a defect was made in the femur. A gelatin sponge, dimensioned at $2 \times 2 \times 10$ mm^3 and preloaded with 0.2 mg of iBP in F127 hydrogel, was positioned onto the defect site and secured with sutures. Two weeks later, the healing progress in both treated and untreated groups was monitored using µCT imaging.

Statistical analysis

Statistical analysis One- or two-way ANOVA followed by Sidak's test for multiple com parisons (with repeated measures for time series data) was used in all studies, as noted in figure legends. For comparison between two groups, Student's *t* tests were performed. All tests used the software GraphPad Prism (GraphPad). The exact p-value is provided in the corresponding figure. For data presented without statistics, the experiment was repeated at least twice to ensure reproducibility, unless otherwise stated.

Reporting summary

Further information on research design is available in the Nature Portfolio Reporting Summary linked to this article.

Data availability

The RNA-seq, and CUT&Tag raw dataset in this study have been deposited in the GEO dataset with accession numbers GSE280429. The remaining data are available within the Article, Supplementary Information or Source Data file. Source data are provided with this paper.

References

1. Hadjidakis, D. J. & Androulakis, I. I. Bone remodeling. *Ann. N. Y. Acad. Sci.* **1092**, 385–396 (2006).
2. Eriksen, E. F. Cellular mechanisms of bone remodeling. *Rev. Endocr. Metab. Disord.* **11**, 219–227 (2010).
3. Dirckx, N., Moorer, M. C., Clemens, T. L. & Riddle, R. C. The role of osteoblasts in energy homeostasis. *Nat. Rev. Endocrinol.* **15**, 651–665 (2019).
4. Wu, Z. et al. Regulation of bone homeostasis: signaling pathways and therapeutic targets. *MedComm (2020)* **5**, e657 (2024).
5. Schupbach, D., Comeau-Gauthier, M., Harvey, E. & Merle, G. Wnt modulation in bone healing. *Bone* **138**, 115491 (2020).
6. Hu, L., Chen, W., Qian, A. & Li, Y. P. Wnt/beta-catenin signaling components and mechanisms in bone formation, homeostasis, and disease. *Bone Res.* **12**, 39 (2024).
7. MacDonald, B. T., Tamai, K. & He, X. Wnt/beta-catenin signaling: components, mechanisms, and diseases. *Dev. Cell* **17**, 9–26 (2009).
8. Gaur, T. et al. Canonical WNT signaling promotes osteogenesis by directly stimulating Runx2 gene expression. *J. Biol. Chem.* **280**, 33132–33140 (2005).
9. Zhang, Y. et al. Co-stimulation of the bone-related Runx2 P1 promoter in mesenchymal cells by SP1 and ETS transcription factors at polymorphic purine-rich DNA sequences (Y-repeats). *J. Biol. Chem.* **284**, 3125–3135 (2009).
10. Hakelien, A. M. et al. The regulatory landscape of osteogenic differentiation. *Stem Cells* **32**, 2780–2793 (2014).
11. Baron, R. & Kneissel, M. WNT signaling in bone homeostasis and disease: from human mutations to treatments. *Nat. Med.* **19**, 179–192 (2013).
12. Moverare-Skrtic, S. et al. Osteoblast-derived WNT16 represses osteoclastogenesis and prevents cortical bone fragility fractures. *Nat. Med.* **20**, 1279–1288 (2014).
13. Zhu, S., Chen, W., Masson, A. & Li, Y. P. Cell signaling and transcriptional regulation of osteoblast lineage commitment, differentiation, bone formation, and homeostasis. *Cell Discov.* **10**, 71 (2024).
14. Dashti, P. et al. Epigenetic regulators controlling osteogenic lineage commitment and bone formation. *Bone* **181**, 117043 (2024).
15. Laugesen, A. & Helin, K. Chromatin repressive complexes in stem cells, development, and cancer. *Cell Stem Cell* **14**, 735–751 (2014).
16. Chiacchiera, F. et al. Polycomb complex PRC1 preserves intestinal stem cell identity by sustaining Wnt/beta-catenin transcriptional activity. *Cell Stem Cell* **18**, 91–103 (2016).
17. Mirzamohammadi, F. et al. Polycomb repressive complex 2 regulates skeletal growth by suppressing Wnt and TGF-beta signalling. *Nat. Commun.* **7**, 12047 (2016).
18. Zhang, B. et al. KDM2B regulates hippocampal morphogenesis by transcriptionally silencing Wnt signaling in neural progenitors. *Nat. Commun.* **14**, 6489 (2023).
19. Wang, J. et al. EED-mediated histone methylation is critical for CNS myelination and remyelination by inhibiting WNT, BMP, and senescence pathways. *Sci. Adv.* **6**, eaaz6477 (2020).
20. Piunti, A. & Shilatifard, A. The roles of Polycomb repressive complexes in mammalian development and cancer. *Nat. Rev. Mol. Cell Biol.* **22**, 326–345 (2021).
21. Zhao, X. & Wu, X. Polycomb-group proteins in the initiation and progression of cancer. *J. Genet Genomics* **48**, 433–443 (2021).
22. Kim, J. J. & Kingston, R. E. Context-specific Polycomb mechanisms in development. *Nat. Rev. Genet* **23**, 680–695 (2022).
23. Tamburri, S., Rustichelli, S., Amato, S. & Pasini, D. Navigating the complexity of Polycomb repression: enzymatic cores and regulatory modules. *Mol. Cell* **18**, 3381–3405 (2024).
24. Farcas, A. M. et al. KDM2B links the Polycomb repressive complex 1 (PRC1) to recognition of CpG islands. *Elife* **1**, e00205 (2012).
25. Wu, X., Johansen, J. V. & Helin, K. Fbxl10/Kdm2b recruits polycomb repressive complex 1 to CpG islands and regulates H2A ubiquitylation. *Mol. Cell* **49**, 1134–1146 (2013).
26. Wu, X. et al. Cooperation between EZH2, NSPc1-mediated histone H2A ubiquitination and Dnmt1 in HOX gene silencing. *Nucleic Acids Res.* **36**, 3590–3599 (2008).
27. Cao, Q. et al. BCOR regulates myeloid cell proliferation and differentiation. *Leukemia* **30**, 1155–1165 (2016).
28. Zhao, W. et al. Essential role for Polycomb group protein Pcgf6 in embryonic stem cell maintenance and a noncanonical polycomb

repressive complex 1 (PRC1) integrity. *J. Biol. Chem*. **292**, 2773–2784 (2017).
29. Scelfo, A. et al. Functional landscape of PCGF proteins reveals both RING1A/B-Dependent-and RING1A/B-independent-specific activities. *Mol. Cell* **74**, 1037–1052.e1037 (2019).
30. Trojer, P. et al. L3MBTL2 protein Acts in concert with PcG protein-mediated monoubiquitination of H2A to establish a repressive chromatin structure. *Mol. Cell* **42**, 438–450 (2011).
31. Zhang, C. et al. Ageing characteristics of bone indicated by transcriptomic and exosomal proteomic analysis of cortical bone cells. *J. Orthop. Surg. Res*. **14**, 129 (2019).
32. Chen, Y. H. et al. Enhancer of zeste homolog 2 and histone deacetylase 9c regulate age-dependent mesenchymal stem cell differentiation into osteoblasts and adipocytes. *Stem Cells* **34**, 2183–2193 (2016).
33. Jing, H. et al. Suppression of EZH2 prevents the shift of osteoporotic MSC fate to adipocyte and enhances bone formation during osteoporosis. *Mol. Ther*. **24**, 217–229 (2016).
34. Krishnamurthy, J. et al. Ink4a/Arf expression is a biomarker of aging. *J. Clin. Invest*. **114**, 1299–1307 (2004).
35. Gearhart, M. D., Corcoran, C. M., Wamstad, J. A. & Bardwell, V. J. Polycomb group and SCF ubiquitin ligases are found in a novel BCOR complex that is recruited to BCL6 targets. *Mol. Cell Biol*. **26**, 6880–6889 (2006).
36. Huo, D. et al. CpG island reconfiguration for the establishment and synchronization of polycomb functions upon exit from naive pluripotency. *Mol. Cell* **82**, 1169–1185.e1167 (2022).
37. Liu, J. et al. Targeting Wnt-driven cancer through the inhibition of Porcupine by LGK974. *Proc. Natl. Acad. Sci. USA* **110**, 20224–20229 (2013).
38. Madan, B. et al. Bone loss from Wnt inhibition mitigated by concurrent alendronate therapy. *Bone Res*. **6**, 17 (2018).
39. Chen, R. et al. Calcium modulates the tethering of BCOR-PRC1.1 enzymatic core to KDM2B via liquid-liquid phase separation. *Commun. Biol*. **7**, 1112 (2024).
40. Wong, S. J. et al. KDM2B recruitment of the polycomb group complex, PRC1.1, requires cooperation between PCGF1 and BCORL1. *Structure* **24**, 1795–1801 (2016).
41. Junco, S. E. et al. Structure of the polycomb group protein PCGF1 in complex with BCOR reveals basis for binding selectivity of PCGF homologs. *Structure* **21**, 665–671 (2013).
42. Cabantous, S. et al. A new protein-protein interaction sensor based on tripartite split-GFP association. *Sci. Rep*. **3**, 2854 (2013).
43. de Castro, K. C. et al. Pluronic(R) triblock copolymer-based nanoformulations for cancer therapy: a 10-year overview. *J. Control Release* **353**, 802–822 (2023).
44. Lippens, E. et al. Cell survival and proliferation after encapsulation in a chemically modified Pluronic(R) F127 hydrogel. *J. Biomater. Appl*. **27**, 828–839 (2013).
45. Akbari, V., Rezazadeh, M. & Ebrahimi, Z. Comparison the effects of chitosan and hyaluronic acid-based thermally sensitive hydrogels containing rosuvastatin on human osteoblast-like MG-63 cells. *Res. Pharm. Sci*. **15**, 97–106 (2020).
46. Khosla, S. & Hofbauer, L. C. Osteoporosis treatment: recent developments and ongoing challenges. *Lancet Diab. Endocrinol*. **5**, 898–907 (2017).
47. Bennett, C. N. et al. Regulation of osteoblastogenesis and bone mass by Wnt10b. *Proc. Natl. Acad. Sci. USA* **102**, 3324–3329 (2005).
48. Kang, S. et al. Wnt signaling stimulates osteoblastogenesis of mesenchymal precursors by suppressing CCAAT/enhancer-binding protein alpha and peroxisome proliferator-activated receptor gamma. *J. Biol. Chem*. **282**, 14515–14524 (2007).
49. Hemming, S. et al. EZH2 and KDM6A act as an epigenetic switch to regulate mesenchymal stem cell lineage specification. *Stem Cells* **32**, 802–815 (2014).
50. Kaneko, S., Son, J., Shen, S. S., Reinberg, D. & Bonasio, R. PRC2 binds active promoters and contacts nascent RNAs in embryonic stem cells. *Nat. Struct. Mol. Biol*. **20**, 1258–1264 (2013).
51. Morey, L. et al. Nonoverlapping functions of the polycomb group cbx family of proteins in embryonic stem cells. *Cell Stem Cell* **10**, 47–62 (2012).
52. Liu, L. et al. Chromatin modifications as determinants of muscle stem cell quiescence and chronological aging. *Cell Rep*. **4**, 189–204 (2013).
53. Yang, N. et al. A hyper-quiescent chromatin state formed during aging is reversed by regeneration. *Mol. Cell* **83**, 1659–1676.e1611 (2023).
54. Malouf, G. G. et al. Architecture of epigenetic reprogramming following Twist1-mediated epithelial-mesenchymal transition. *Genome Biol*. **14**, R144 (2013).
55. Basenko, E. Y. et al. Genome-wide redistribution of H3K27me3 is linked to genotoxic stress and defective growth. *Proc. Natl. Acad. Sci. USA* **112**, E6339–E6348 (2015).
56. Klauke, K. et al. Polycomb Cbx family members mediate the balance between haematopoietic stem cell self-renewal and differentiation. *Nat. Cell Biol*. **15**, 353–362 (2013).
57. Sparbier, C. E. et al. Targeting Menin disrupts the KMT2A/B and polycomb balance to paradoxically activate bivalent genes. *Nat. Cell Biol*. **25**, 258–272 (2023).
58. Fan, Z. et al. BCOR regulates mesenchymal stem cell function by epigenetic mechanisms. *Nat. Cell Biol*. **11**, 1002–1009 (2009).
59. Zhang, P. et al. Loss of Asxl1 alters self-renewal and cell fate of bone marrow stromal cell, leading to bohring-opitz-like syndrome in mice. *Stem Cell Rep*. **6**, 914–925 (2016).
60. Ismail, I. H., McDonald, D., Strickfaden, H., Xu, Z. & Hendzel, M. J. A small molecule inhibitor of polycomb repressive complex 1 inhibits ubiquitin signaling at DNA double-strand breaks. *J. Biol. Chem*. **288**, 26944–26954 (2013).
61. Shukla, S. et al. Small-molecule inhibitors targeting Polycomb repressive complex 1 RING domain. *Nat. Chem. Biol*. **17**, 784–793 (2021).
62. Banito, A. et al. The SS18-SSX oncoprotein Hijacks KDM2B-PRC1.1 to drive synovial sarcoma. *Cancer Cell* **33**, 527–541 e528 (2018).
63. van den Boom, V. et al. Non-canonical PRC1.1 targets active genes independent of H3K27me3 and is essential for leukemogenesis. *Cell Rep*. **14**, 332–346 (2016).
64. Declercq, H. et al. Isolation, proliferation and differentiation of osteoblastic cells to study cell/biomaterial interactions: comparison of different isolation techniques and source. *Biomaterials* **25**, 757–768 (2004).
65. Zhou, Y. et al. Metascape provides a biologist-oriented resource for the analysis of systems-level datasets. *Nat. Commun*. **10**, 1523 (2019).
66. Dong, F. et al. ALKBH5 facilitates hypoxia-induced paraspeckle assembly and IL8 secretion to generate an immunosuppressive tumor microenvironment. *Cancer Res*. **81**, 5876–5888 (2021).
67. Li, R. et al. Generation and validation of versatile inducible CRISPRi embryonic stem cell and mouse model. *PLoS Biol*. **18**, e3000749 (2020).
68. Dai, Z. et al. Inducible CRISPRa screen identifies putative enhancers. *J. Genet Genomics* **48**, 917–927 (2021).
69. Zheng. G. et al. Topographical cues of direct metal laser sintering titanium surfaces facilitate osteogenic differentiation of bone marrow mesenchymal stem cells through epigenetic regulation. *Cell Prolif*. **51**, e12460 (2018).

Acknowledgements

We thank the Core Facility of Research Center of Basic Medical Sciences, high performance computing (HPC) platform at Tianjin Medical University for technical support. The Wnt reporter construct was provided by Dr. Chunsheng Kang, TMU General Hospital. This study was supported by by the National Key R&D Program of China (2024YFA1802300 to X.W., 2019YFA0112100 to S.F., 2022YFA1303101 to J.L.), National Natural Science Foundation of China (32320103009, 82473964 to X.W.; 82071079 to D.L.), The Key Program of Tianjin Natural Science Foundation (23JCZDJC00210 to D.L.), Jinmen Medical Talents Project of Tianjin Health Commission (TJSJMYXYC-D2-025 to D.L.), Basic Research Project of Guangzhou Institutes of Biomedicine and Health, Chinese Academy of Sciences (GIBHBRP24-04 to Y.X. and J.X.) and National Youth Yalent Support Program (X.W.).

Author contributions

Conceptualization: D.L., X.W., J.L. Methodology: Z.O., X.L. (Xuan Li), S.T., Y.C., B.F. Investigation: L.X., J.X., M.G., Y.L., L.M., R.D., Y.Z., X.L. (Xu Liu), C.L., F.G., R.H., H.S., Y.D., Y.X., T.L., Y.Z., and L.S. Analysis of data: L.X., H.C. Funding acquisition: S.F. Supervision: S.F., J.L., D.L., X.W. Writing – original draft: L.X., X.W. Writing – review & editing: J.X., M.G., Y.L., D.L., X.W.

Competing interests

The authors declare no competing interests.

Ethics statement

We support inclusive, diverse, and equitable conduct of research.

Additional information

Supplementary information The online version contains supplementary material available at https://doi.org/10.1038/s41467-025-59638-w.

Correspondence and requests for materials should be addressed to Shiqing Feng, Jinsong Liu, Dayong Liu or Xudong Wu.

Peer review information *Nature Communications* thanks the anonymous reviewers for their contribution to the peer review of this work. A peer review file is available.

Reprints and permissions information is available at http://www.nature.com/reprints

---

[1]State Key Laboratory of Experimental Hematology, The Province and Ministry Co-sponsored Collaborative Innovation Center for Medical Epigenetics, Key Laboratory of Immune Microenvironment and Disease (Ministry of Education), Tianjin Key Laboratory of Medical Epigenetics, Department of Endodontics, Tianjin Medical University School and Hospital of Stomatology & Tianjin Key Laboratory of Oral Soft and Hard Tissues Restoration and Regeneration, Tianjin Medical University, Tianjin, China. [2]Department of Cell Biology, Tianjin Medical University, Tianjin, China. [3]China-New Zealand Joint Laboratory on Biomedicine and Health, Guangzhou Institutes of Biomedicine and Health, Chinese Academy of Sciences, Guangzhou, China. [4]Institute of Drug Discovery, Guangzhou Institutes of Biomedicine and Health, Chinese Academy of Sciences, Guangzhou, China. [5]State Key Laboratory of Respiratory Disease, Guangzhou Institutes of Biomedicine and Health, Chinese Academy of Sciences, Guangzhou, China. [6]Department of Medicinal Chemistry, Tianjin Key Laboratory on Technologies Enabling Development of Clinical Therapeutics and Diagnostics, School of Pharmacy, Tianjin Medical University, Tianjin, China. [7]International Science and Technology Cooperation Base of Spinal Cord Injury, Department of Orthopedic Surgery, Tianjin Medical University General Hospital, Tianjin, China. [8]The Second Hospital, Cheeloo College of Medicine, Shandong University, Jinan, China. [9]Shanghai Engineering Research Center of Tooth Restoration and Regeneration & Tongji Research Institute of Stomatology & Department of Endodontics, Shanghai Tongji Stomatological Hospital and Dental School, Tongji University, Shanghai, China. [10]These authors contributed equally: Liangyu Xing, Jinxin Xu, Meihan Gong, Yunzhi Liu. ✉e-mail: sqfeng@tmu.edu.cn; liu_jinsong@gibh.ac.cn; dyliuperio@tmu.edu.cn; wuxudong@tmu.edu.cn